CRITICAL REVIEWS IN SOLID STATE AND MATERIALS SCIENCES
https://doi.org/10.1080/10408436.2025.2503148

Taylor & Francis
Taylor & Francis Group

REVIEW ARTICLE

OPEN ACCESS Check for updates

From metallic liquids to metallic glasses: *in-situ* monitoring the atomic structure evolution by synchrotron X-ray diffraction

Martin E. Stiehler and Konstantinos Georgarakis

Faculty of Engineering and Applied Sciences, Cranfield University, Cranfield, UK

ABSTRACT

Although ubiquitous in nature and technology, a deep understanding of glass formation and glass transition is still missing. It is assumed that the remarkable slowdown of kinetics towards vitrification can be traced back to structural changes in the undercooled liquid. Therefore, a continuous monitoring of the atomic structure during cooling from the equilibrium liquid to the glass is inevitable. However, the high critical cooling rates usually necessary for vitrification of metallic alloys make this a challenging, but at the same time very exciting, endeavor. Only in recent years, it has been technologically possible to achieve *in-situ* monitoring of the evolving structure for a small number of metallic-glass-forming alloys. Currently, only high-energy X-rays from synchrotron sources as probes in combination with fast two-dimensional detectors can capture diffraction images from usually containerlessly levitated samples with the necessary scattered intensity as well as resolution in space and time. Here, results for those materials where in-situ monitored vitrification has been experimentally accomplished are reviewed, and approaches to experiment and data processing are compared. Insights into the structural behaviour during vitrification derived from these experiments are discussed. Results from accompanying simulations are also included. In addition to the in-situ observation of vitrification, structural indications of possible liquid-liquid crossovers in the alloys are considered as well.

KEYWORDS

Glass-forming ability; glass transition; liquid-liquid transitions; synchrotron radiation; in-situ diffraction; vitrification; containerless levitation; rapid solidification

Table of contents

1. Introduction 1
2. Experimental methods 4
2.1. Levitation techniques 4
2.2. Scattering techniques 7
3. Structural functions 9
4. Data acquisition and reduction 10
5. Data analysis 10
6. The pathway 13
6.1. Undercooling 13
6.2. Liquid-liquid crossovers 17
6.3. Vitrification 19
7. Outlook 20
Disclosure statement 23
References 23

1. Introduction

When undercooled fast enough below its liquidus temperature T_l, crystallisation of a melt can be avoided, and a solid with an amorphous structure, known as glass, can be formed. While in terms of the atomic structure a relatively easy distinction between crystal and liquid can be made, the difference between a glass and a liquid is not equally as straightforward. It can be speculated that, 25 years ago, it was this structural similarity between glass and liquid that led

CONTACT Martin E. Stiehler martin.stiehler@cranfield.ac.uk

© 2025 The Author(s). Published with license by Taylor & Francis Group, LLC.
This is an Open Access article distributed under the terms of the Creative Commons Attribution License (http://creativecommons.org/licenses/by/4.0/), which permits unrestricted use, distribution, and reproduction in any medium, provided the original work is properly cited. The terms on which this article has been published allow the posting of the Accepted Manuscript in a repository by the author(s) or with their consent.

P.W. Anderson to consider the glass transition one of the deepest unsolved problems in solid-state theory.[1] Despite considerable progress, many aspects of the puzzle remain unsolved till today. Due to their growing technological relevance[2–7] the origin of the high glass-forming ability (GFA) of bulk-metallic glasses (BMG) is of great interest.

Although a glass can be formed from a melt by rapid temperature decrease (quenching), rapid pressure increase (crushing), or a combination of both (crunching)[8] this review addresses glass formation and glass transition by quenching a metallic melt only. The glass transition, taking place at the glass-transition temperature T_g, in the direction from high to low temperatures, is referred to as *vitrification* (liquid-to-glass transition). It should be noted that, although logically sound, the transition in the opposite direction, i.e., the transition from the glass to the liquid, is generally *not* called "devitrification." This term is usually reserved for the crystallisation of a glass by ageing or other influences. More generally, the term "glass" will be used here for an amorphous solid irrespective of its origin (i.e., not only when originating from a liquid), and the term "amorphous" in relation to the atomic structure (i.e., applicable for the equilibrium liquid above T_l and the undercooled liquid below T_l as well as the glass).

To get deeper insights into subtle structural differences between liquid and glass, data with high resolution in space as well as time are needed. The high temporal resolution is necessary since experiments need to be carried out under rapid cooling dictated by the high critical cooling rates to bypass crystallisation. Furthermore, since important processes related to glass formation already take place above T_l,[9] the structural investigation should commence at sufficiently high temperatures.

To avoid heterogeneous crystallisation, containers must be abandoned in most cases, and levitation techniques need to be employed. As will be discussed in more detail in Section 2, from several levitation techniques available, only electrostatic levitation (ESL) and aerodynamic levitation, the latter usually in the form of conical nozzle levitation (CNL), are used for the study of metallic glasses. From the palette of structural probes (electron, neutron and X-ray diffraction), only X-ray diffraction (XRD) is currently able to serve the necessary speed, intensity and resolution for monitoring the structural changes in the systems under investigation. The underlying reasons will be elaborated on in Section 2 together with a short outline of the experimental methods, while detailed reviews of the latter can be found elsewhere.[10–14]

In combination, the aforementioned prerequisites mandate that the complete pathway (or at least major parts of it) starting from the equilibrium liquid, during undercooling and vitrification to the glass (Figure 1) has to be continuously monitored *in situ* by high-energy synchrotron X-ray diffraction in transmission mode using containerlessly levitated samples. For the remainder of this review, the term *pathway* refers to the sequence just described. In particular, wide-angle X-ray scattering (WAXS) is used to resolve the structure in appropriate detail. This article seeks to review the key results of studies that investigated metallic alloys in this manner. In parallel to the metallic melts, several oxides have been monitored in the same way.[19,20] Despite some similarities with metallic materials oxides will not be discussed in detail here. More information can be found in recent review articles.[11,12,21] The feasibility of other spectroscopic techniques to monitor the pathway, e.g., SAXS (small-angle X-ray scattering), AXS (anomalous X-ray scattering) and EXAFS (extended X-ray absorption fine structure) as well as, e.g., electron scattering, is briefly discussed in Section 2 and the Outlook (Section 7), respectively. Further quantities like electrical resistivity[22,23] or specific heat[18] have also been monitored *in situ* in levitation experiments and show characteristic changes around T_g.

Along this pathway, it is not only the in-situ observation of vitrification itself that is of interest, but also other phenomena which are possibly linked to liquid-liquid crossovers (LLC) and are often associated with so-called fragile-to-strong crossovers (FSC).[24–26] Here, LLCs, as they may show in in-situ structural measurements, will be addressed rather than providing an in-depth investigation of their still not well-understood nature in general as well as in metallic-glass-forming liquids in particular. LLCs have recently been reviewed,[26–29] and a lot of theoretical work has been dedicated to the possible descriptions of LLCs in a unified manner.[30–32] Different designations found in literature, like liquid-liquid transitions (LLT) or liquid-liquid phase transitions (LLPT), will be summarised under the more circumspect term LLC since it is unclear to what extent they can be considered thermodynamic transitions. The possible location of an LLC in a TTT (time-temperature-transformation) diagram is roughly sketched in (Figure 1a).

The first in-situ diffraction study along the complete pathway for metallic alloys was reported for $Pd_{40}Cu_{30}Ni_{10}P_{20}$ in 2003 by Uriarte et al. in the group of A.R. Yavari in Grenoble[33] (Figure 2). Although since then a few further in-situ monitored vitrifications

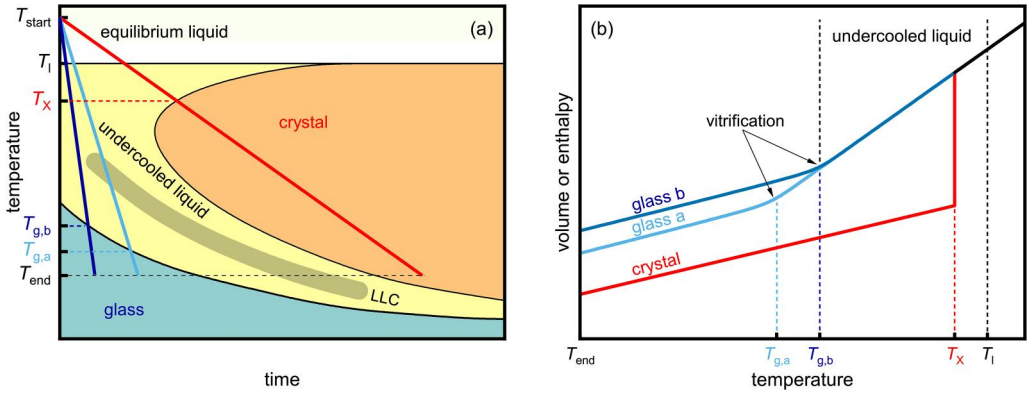


Figure 1. Schematic time-temperature-transformation (TTT) diagram of a model alloy quenched from T_{start} (well above the liquidus temperature T_l or melting temperature T_m in case of a eutectic alloy) with three different cooling rates (a) and the temperature dependence of its volume or enthalpy at constant pressure (b). The model experiment ends at T_{end}. Depending on the cooling rate the (undercooled) liquid can crystallise at T_X (red) or vitrify at different glass transition temperatures $T_{g,a}$ (light blue) or $T_{g,b}$ (dark blue) yielding glasses with slightly different properties (it needs to be mentioned that T_X depends on the cooling rate as well and also differs from a T_X upon heating the glass). Pathway b passes through a possible liquid-liquid crossover (LLC). Its range of existence and transition region is often only insufficiently known and, therefore, only roughly sketched in (a) (shaded in grey). The effects of LLCs on the macroscopic sample volume are controversial[15–18] and have been omitted in (b).

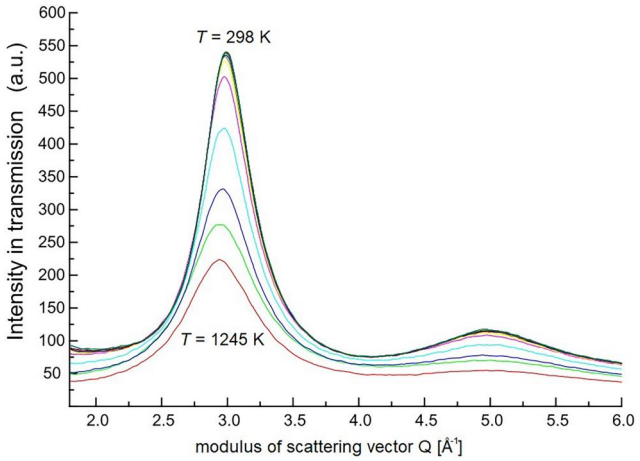


Figure 2. Intensity distribution $I(Q)$ acquired using high-energy synchrotron X-ray diffraction in transmission at various temperatures for the first reported in-situ monitoring of the complete pathway from the equilibrium liquid down to the glass for metallic alloys ($Pd_{40}Cu_{30}Ni_{10}P_{20}$, $T_l = 864$ K, $T_g = 569$ K)[33] (reproduced with permission from ref. [34]).

of BMGs were reported (Table 1), a first detailed analysis including many structural metrics derived from the experimentally obtained structural functions (Section 3) and supporting comprehensive results from computer simulations was not published until 2015 for $Zr_{60}Cu_{30}Al_{10}$.[45]

It is necessary to mention that in parallel to in-situ monitoring of structural metrics during cooling, annealing of metallic glasses also progressed.[34,35,47–53] Mainly performed on melt-spun samples, these investigations complement the in-situ cooling experiments, especially when performed for the same composition. The major drawback of experiments in annealing mode is the wide temperature range in which the alloy *cannot* be monitored in an amorphous regime due to the intervention of crystallisation (i.e., $T_X < T < T_l$). If the sample is annealed to temperatures above T_g, but below T_X, technically in-situ vitrification ("re-vitrification" for that matter) can be monitored on cooling to temperatures below T_g.[54–58] Since this review is dedicated to studies of the complete pathway, reports on such re-vitrifications are not reviewed here. Nevertheless, re-vitrification studies can help investigate cooling-rate dependencies of the structure for deeply undercooled samples.[58] Furthermore, being able to perform heating and cooling, i.e., cycling the same sample, in the same setup opens the opportunity to explore possible hystereses of the temperature-dependent structural changes. crystallisation of metallic glasses upon heating (and slow cooling) is in itself of utmost interest, and the occurrence of different phases depending on the heating or cooling rate is of relevance for basic research as well as for possible applications of metallic glasses.[59–61] Comparing the structure of an alloy slightly above and below T_g structural changes seem to be extremely minute. However, tracing the structure in a certain temperature interval around and during the glass transition (in either direction), marked changes ("kinks") in the temperature dependence of structural metrics become clear indicating its structural basis. Despite a lot of progress in experimental techniques, still only a few BMG-forming alloys have been analysed in situ along the complete pathway to date.

Table 1. Some key data for the metallic alloys that have been successfully vitrified under *in-situ* structural monitoring by high-energy synchrotron X-rays: the temperature interval during which *in-situ* monitoring took place, the glass-transition temperature T_g, the liquidus temperature T_l, the reduced glass-transition temperature T_g/T_l, the onset temperature of a possible LLC T_{LLC} (this quantity may be denoted differently in the individual references), the ratio T_{LLC}/T_g, the method of sample mounting (amp: quartz *amp*oule), the method of heating (L: laser, I: inductive heating), the achieved cooling rates and method as given in the reference and (a: air jet on outside of quartz ampoule after stopping induction current; n: using liquid nitrogen instead of air; f: free cooling after switching-off laser causing a strongly temperature-dependent cooling rate; c: controlled cooling using the heat source to achieve a particular cooling rate), the energy E_i and wavelength λ_i of the incident monochromatic high-energy X-ray beam and the year of the report as referenced.

Alloy	T interval K	T_g K	T_l K	$\frac{T_g}{T_l}$	T_{LLC} K	$\frac{T_{LLC}}{T_g}$	Mount/heat	Cooling rate K/s	E_i (λ_i) keV (Å)	Year/ref.
$Pd_{40}Cu_{30}Ni_{10}P_{20}$	1270 … 600	569[35]	864[35]	0.659	–	–	amp/I	30 … 10 (a)	90 (0.138)	2003[33]
$Pd_{40}Cu_{30}Ni_{10}P_{20}$	910 … 298	569[35]	864[35]	0.659	–	–	amp/I	8.33 avg. (n)	92.5 (0.134)	2011[35,36]
$Pd_{42.5}Cu_{30}Ni_{7.5}P_{20}$	1100 … 420	575[36]	836[36]	0.688	–	–	ESL/L	5…0.5 (f)	131 (0.095)	2019[37]
$Zr_{50}Cu_{40}Al_{10}$	1700 … 700	712[38]	1159[38]	0.614	–	–	CNL/L	120 avg. (f)	113.4 (0.109)	2010[39]
$Zr_{50.7}Cu_{28}Ni_9Al_{12.3}$	1673 … 673	– †	1167	–	–	–	CNL/L	84 avg. (c)	61.67 (0.201)	2012[40]
$Zr_{51.9}Cu_{23.3}Ni_{10.5}Al_{14.3}$	1673 … 673	776	1132	0.686	–	–	CNL/L	97 avg. (c)	61.67 (0.201)	2012[40]
$Zr_{55}Cu_{30}Ni_5Al_{10}$	1346 … 388	683[41]	1150[41]	0.594	–	–	CNL/L	85 avg. (f)	100 (0.124)	2020[42]
$Zr_{57}Cu_{15.4}Ni_{12.6}Al_{10}Nb_5$	1389 … 577‖, §	682	1115	0.612	1000	1.47	ESL/L	4.3 avg. (f)	129 (0.096)	2016[43]
$Zr_{58.5}Cu_{15.6}Ni_{12.8}Al_{10.3}Nb_{2.8}$	1473 … 673	708†, ‡[44]	1170	0.605	∼ 860	1.21	ESL/L	5 avg. (f)	100 (0.124)	2016[18]
$Zr_{60}Cu_{30}Al_{10}$	1471 … 372	671	1207	0.556	1070	1.59	CNL/L	100 avg. (f)	100 (0.124)	2015[45]
$Ti_{40}Cu_{34}Pd_{14}Zr_{10}Sn_2$	1473 … 487	689	1176	0.586	–	–	CNL/L	80 avg. (f)	100 (0.124)	2025[46]

† T_g not identifiable in metrics
‡ Vitrification not discussed
‖ Cooling started at 1678 K
§ Minor crystallinity below 850 K

These alloys are listed in Table 1 together with the studied temperature range and some key experimental parameters. The immense experimental effort is the main factor limiting the number of such studies. Another one is the need for sufficiently high GFA, which reduces the number of alloys or alloy systems that can currently be studied in the way reviewed here. Nevertheless, insights towards the identification of possible universal trends can already be derived.

The remainder of this article is organised as follows. In Section 2 the experimental methods outlined above are described in more detail, followed by a brief description of the theoretical background for elastic scattering (Section 3). Section 4 presents a few details about processing raw data and the necessary software, while Section 5 describes further steps of data treatment, how structural metrics can be obtained from the experimental data, fitting and ways of presenting data. In Section 6 results for milestones standing along the pathway, as reported by the different authors, are discussed. An outlook to the future of the field is given in Section 7.

2. Experimental methods

To accomplish in-situ vitrification, sufficiently high cooling rates as well as the exclusion of all sources of heterogeneous nucleation need to be achieved. The necessary cooling rate is dictated mainly by the critical cooling rate of the material itself. The cooling rate can be reduced by actively heating the sample during otherwise free cooling. A higher cooling rate can be achieved by a smaller sample size, which, however, may be detrimental to sample handling. Heterogeneous nucleation can only be avoided by the omission of a sample container. This immediately implies the need for a means of levitation of the sample during (ground-based) experiments as well as the avoidance of any other reactive environment. For the same reason, temperature measurements need to be taken contactlessly. Therefore, one or more optical pyrometers are used.[10,19,45,62,63] At low temperatures they become ineffective and can be replaced by infrared pyrometers.[12,62,64] Alternatively, an extrapolation to lower temperatures can be made by assuming and fitting an exponential function to the temperature profiles $T(t)$ (time-dependent surface temperature of the sample) measured at high temperatures.[45] These methods can be used for all levitation methods discussed here. After introducing the levitation methods the relevant diffraction techniques for structure determination are briefly addressed.

2.1. Levitation techniques

Of the possible levitation techniques[14,65] three are usually used for structural studies on macroscopic metallic-glass samples, which are electromagnetic levitation (EML), electrostatic levitation (ESL) and aerodynamic levitation, the latter mainly in the form of conical nozzle levitation (CNL). Detailed reviews can be found in the literature.[12,14,66–70] Each method has certain advantages and disadvantages in relation to

the measurements taken, and not all are suitable for in-situ monitoring of temperature-dependent fast structural changes. The method used also depends on the material to be investigated, especially its GFA, as well as sample size. While ESL and CNL allow for diameters of about 3 mm, EML can be used for diameters twice as big.[65]

The oldest of these techniques is *electromagnetic levitation* (EML).[71] Its relatively simple basic construction consists of a coil-shaped, water-cooled metallic pipe (Figure 3). A traversing alternating electrical current generates an electromagnetic field, which, in turn, will induce currents inside a conductive material (sample) placed in the centre of the coil. These currents will generate a secondary magnetic field, which causes the sample to levitate inside the coil (Lenz's law).

At the same time, the induced currents also heat the sample beyond T_l. What seems to be convenient at first glance prevents this method from being used for the desired temperature-dependent measurements of the necessary wide temperature range considered here since heating and stable levitation would not be as independent of each other as necessary. Especially at low temperatures (e.g., below T_g), levitation is still necessary while heating is not. Although there are ways to mitigate this issue, e.g., by a combination with aerodynamic levitation[69,72] this method has not been used for any of the metallic glasses considered in this thesis (Table 1). Due to the need for electrically conductive materials, EML cannot be used for oxide glasses either. Other problems like sample deformation need to be considered as well[72] which may hamper accurate temperature measurements or even prevent the desired deep undercooling by premature nucleation.[73]

Electrostatic levitation (ESL) in principle dates back to the experiments of Millikan published in 1911, where small levitated charged oil drops were used to determine the elementary electrostatic charge.[74] Studying undercooling and recalescence of large samples of high-temperature materials, ESL was used only about 80 years later[73] followed by the first X-ray scattering studies on electrostatically levitated metallic liquids another decade thereafter.[75] Finally, temperature-dependent measurements over a wide temperature range and in-situ vitrification were performed using ESL only recently (Table 1). Compared to EML, the use of ESL has some key advantages. The range of materials that can be studied with this method spans metals, semiconductors and insulators, since the only requirement to generate a levitation force is a sufficient surface charge which is created by the photoelectric effect[13] using ultraviolet light or by thermionic emission.[76] For ESL, sample heating and levitation are independent of each other, making a wide temperature range accessible, while feedback control provides a stable sample positioning throughout the experiments.[77] Furthermore, no distortion of molten samples occurs (Figure 4).

While for EML the heating and levitation coil blocks the unrestricted view to the sample from the majority of angles, for ESL an open view for a plethora of instruments around the sample is possible, allowing a variety of measurements and diagnostics to take place simultaneously.[73,78] Those experiments can comprise density and thermal expansion by measuring the temperature-dependent size of the levitated ball using cameras and appropriate lighting,[15,17,79] measuring the temperature-dependent specific heat and emissivity utilising the Stefan-Boltzmann law,[80,81] or even measurements of the viscosity or surface tension by adding a

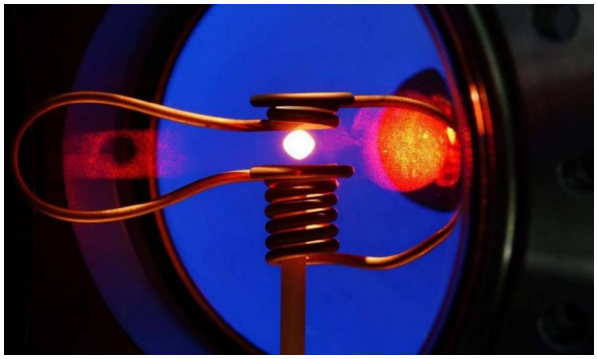


Figure 3. Electromagnetically levitated metallic droplet (centre) inside the coil responsible for levitation and heating (reproduced with permission from ref. [13]).

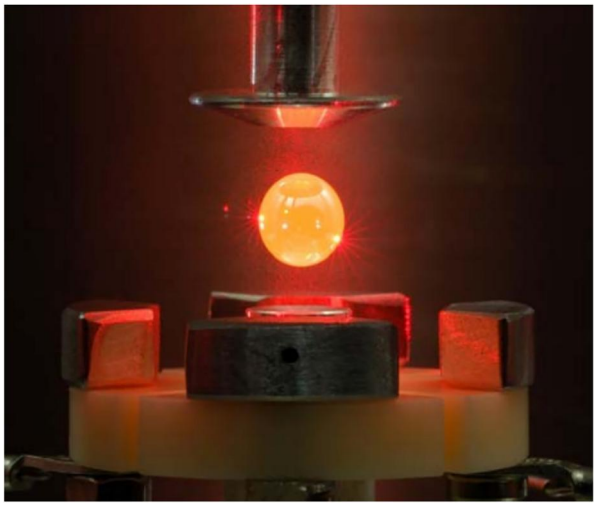


Figure 4. Electrostatic levitation exemplified for 0.6 g of liquid $Ti_{39.5}Zr_{39.5}Ni_{21}$ (centre) at 1150 K (reproduced with permission from ref. [71]).

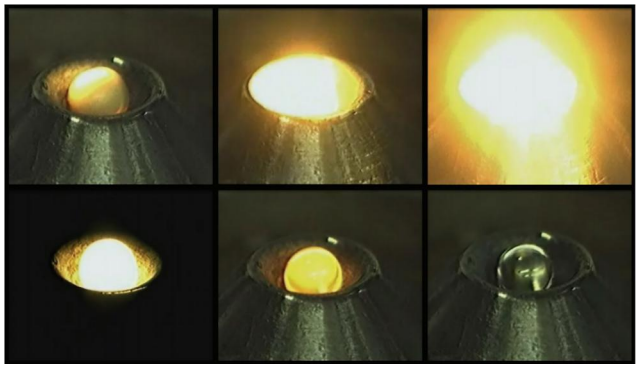


Figure 5. *In-situ* vitrification in a CNL setup showcased for an oxide melt (reproduced from ref. [11]). From top left to bottom right, the sample is heated and melted and subsequently vitrifies during cooling.

sinusoidal electric field to the levitation field for a short time[76,82] and observing the time-dependent ring-down of the surface oscillations. Alternatively, the shape change of the drop upon rotation can be analysed to determine surface tension.[83,84]

The independence of levitation and heating requires an independent source for sample heating for which different types and numbers of lasers are used. By varying their output power, the temperature of the sample can be adjusted without impeding sample levitation. In-situ vitrification usually demands a cooling rate as high as possible if not only materials with exceptionally high GFA are to be investigated. Since ESL needs to take place in vacuo to prevent electrical breakdowns,[77] cooling is possible by radiation only, which limits the possible cooling rates $\dot{T}(t)$. The highest $\dot{T}$ is achieved by free cooling after switching off the lasers completely. Despite many advantages, this considerably limits the number of alloys for which in-situ monitoring of vitrification is possible in an ESL setup to those with exceptionally high GFA. Especially at low temperatures, the small cooling rates cause cooling to become slow, i.e., the cooling curve $T(t)$ becomes very flat and a reliable assignment of a temperature to a diffraction image is hampered. In this case, even for samples with low critical cooling rates in-situ vitrification was not described, although no crystallisation took place.[17,18]

The lasers used for heating vary in type, number and position relative to the sample[84] where wavelengths in the infrared part of the spectrum are preferred. Asymmetric heating, e.g., by using only one laser beam on top of the sample, can be used for interesting effects like "polyamorphic rotors" in connection with LLCs.[85] With isotropic laser heating sample temperatures of 3000 K and beyond can be reached.[76,86,87] However, this may cause evaporation of sample material and possible changes in composition, which need to be verified by weighing the sample and chemical analysis after the experiment. Furthermore, coating of the pyrometer window in the vacuum chamber with sample material and possibly distorted temperature readings need to be considered and measures to mitigate them to be employed.[13] Aerodynamic levitation suffers less from this issue than EML and ESL.

Figures 5 and 6 show the shape of the nozzle that provided the name *conical nozzle levitation* (CNL) for this almost exclusively used design in state-of-the-art *aerodynamic-levitation* setups.[10,13,62,88–91]

Based on the early works of Winborne et al.,[92] the nozzle design has improved over time to allow increasingly bigger portions of the sample to be visible to the neutron or X-ray beam as well as to diagnostic instruments.[12] Metallic-glass samples are stably levitated by a regulated flow of inert gas, usually Ar, through a convergent-divergent conical nozzle channeled upwards to counteract gravity.[13] Levitation can be acoustically stabilised.[93–95] Technically, CNL is not a containerless method. However, the use of noble gases should sufficiently exclude reactions causing heterogeneous nucleation. Like for ESL, levitation and heating are independent of each other for CNL as well, and laser heating is performed in a virtually identical way as compared to ESL. The big difference and major advantage compared to, e.g., ESL is that the levitation gas also provides a drastic increase in cooling rate, making it possible to observe in-situ vitrification for a much wider range of liquids compared to the other levitation methods. Although it would provide an even higher thermal conductivity and subsequently higher cooling rates,[23,96] it is less suitable for CNL,[97] mainly due to small atomic mass. Furthermore, the levitation gas also reduces sample evaporation (and coating of windows and other components).[12] Minor drawbacks of CNL can be seen in additional scattering from the levitation gas and the lower suitability for experiments that involve oscillations of the molten material (e.g., for surface tension). However, if the main goal of the investigation is to acquire structural information over a wide temperature range along the pathway, including deep undercooling and vitrification, CNL can be considered the best choice.

Containerless processing would be eminently facilitated if the need to counteract gravity is largely reduced or completely removed. Accordingly, experiments in microgravity have been performed during parabola flights, on board sounding rockets, on the Space Shuttle or on the International Space Station

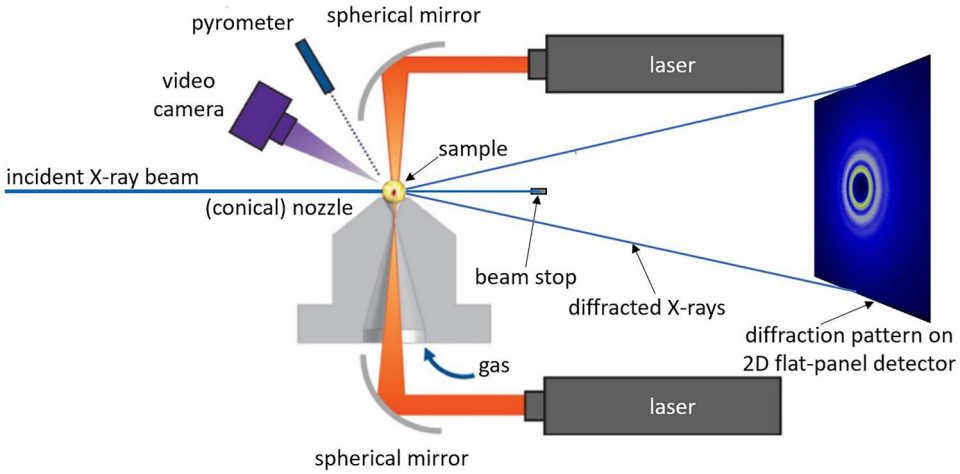


Figure 6. Schematic representation of conical-nozzle levitation and laser heating for synchrotron X-ray diffraction (adapted with permission from ref. [13]).

(ISS).[22,23,66,77,96,98–102] For sample stabilisation and positioning, combinations with the aforementioned techniques are possible.[100] Microgravity, furthermore, allows for measuring bigger samples than in ground-based setups,[70,99,100] the spherical shape and surface of the droplets are less disturbed, and convection is greatly reduced.[22] However, due to the lack of compact radiation sources with the necessary characteristics, it is currently not possible to perform structural investigation in these environments.[98,103–105] Measurements in reduced gravity are therefore restricted to containerless measurements of density, thermal expansion, viscosity, surface tension, heat capacity or electrical resistivity – the latter being at least an indirect scattering experiment using the conduction electrons as a probe.

Ground-based levitation setups were first used to determine aforementioned macroscopic quantities like density, thermal expansion coefficient, heat capacity, emissivity, surface tension and viscosity[79,106] that can be inferred directly by observing the entire levitated sample, e.g., by using cameras. For the observation of the atomic structure and its evolution, probes sensitive to interatomic distances are necessary. To gain insights into the bulk of the sample, rather than their surface, appropriate diffraction experiments are needed, which, however, yield information in *reciprocal space* only. *Real space* information needs to be reconstructed subsequently, which relates to several challenges on its own, as outlined in Section 3. The methods for determination of the atomic structure are briefly discussed in the following.

2.2. Scattering techniques

The scattering techniques commonly used in condensed-matter science are X-ray, neutron and electron diffraction. To gain information not only on the average structure, but also on the compositionally resolved *partial structure factors* or *pair correlation functions* in non-monatomic materials the same sample would need to be investigated by more than one of these probes.[107] Given the usually high number of elements in BMGs with high GFA not enough independent scattering techniques may be available. The situation becomes even more aggravated since the high critical cooling rates demand an ultrafast operation and detection mode with a high frame rate for all of them. A single frame captured needs to contain a complete diffraction pattern. However, the higher the frame rate the less "light" enters the detector per frame and the lower the signal-to-noise ratio (SNR) becomes. All these considerations favour a transmission geometry with source, sample and (two-dimensional) detector being in one line and stationary (Figures 6 and 7).

Since sample handling for levitation and the necessary cooling rates call for millimetre-sized samples the probe needs to be able to penetrate balls of according to diameters. This immediately excludes the use of electron diffraction since even with energies in the MeV range electrons can only penetrate samples with diameters < 1 μm,[109–111] not to mention the levitation gas surrounding the sample. Furthermore, in contrast to neutrons and X-ray photons, electrons carry electric charge, i.e. electron diffraction would be excluded even in a reflection geometry due to distortion of the incident beam by the magnetic and electric fields used for EML and ESL as well as the charged levitating sample itself. Although millimetre-sized samples are unproblematic for neutrons to be penetrated it is the low achievable intensity and the necessary high acquisition times that exclude this type of radiation. Possible ways to mitigate these problems are

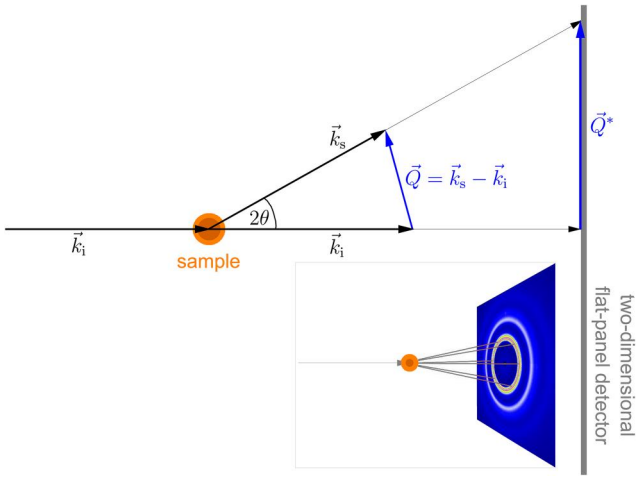


Figure 7. Geometry for elastic scattering methods in transmission. In case of a 2D flat-panel detector the scattering vector $\vec{Q}$ has to be calculated from its projected version $\vec{Q}^*$. The scattering vector $\vec{Q}$ "translates" the incident wavevector $\vec{k}_i$ to the wavevector $\vec{k}_s$ of the wave scattered elastically at scattering angle 2θ, where $|\vec{k}_s| = k_s = k_i = |\vec{k}_i|$. The inset (adapted from ref. [108]) sketches a slanted view on the geometry illustrating the relation of sample, beams and diffraction pattern.

discussed in Section 7. Thus, the current state of technology only allows high-energy (synchrotron) X-rays to be used as structural probe to gain the wanted insights into metallic-glass-forming alloys. With the term "high-energy" commonly used for energies $E_i > 60$ keV of the incident monochromatic X-ray beam[11] all experiments listed in Table 1 fall into this category (for comparison the frequently used Cu- K_α radiation from a typical laboratory X-ray source has a wavelength $\lambda_i \approx 1.54$ Å corresponding to $E_i = 8.05$ keV). State-of-the-art sources of this kind of radiation are synchrotrons now available in different places around the globe. Only due to the high brilliance and high energy of synchrotron light sources it has been possible to reduce acquisition times by obtaining 2D-diffraction patterns with enough intensity per frame.[33,112] Details of X-ray generation in synchrotrons can be found elsewhere.[113] Close to absorption edges of a specific given element its atomic form factor changes anomalously.[112,114] Comparing scattering patterns using incident X-rays with energy close to such an absorption edge with those using energy away from it a substantial contrast can be found. Harnessing this effect the so-called anomalous X-ray scattering (AXS) technique provides element-selective information that can be used to disentangle partial structure factors.[107,114] Different X-ray energies can so be considered as independent types of radiation. Although AXS has been widely used for amorphous materials (liquid and glass) at constant temperature[112,114–118] a temperature-dependent study of the pathway or parts thereof is missing so far. To achieve an accurate disentanglement experiments using different incident energies would need to be carried out at the same sample either simultaneously, which would be related to a very complex experimental setup that is not available to date, or in consecutive runs with all other parameters exactly reproduced (cf. Section 7). Another well-known element specific synchrotron X-ray method, EXAFS (extended X-ray absorption fine structure),[119,120] although fast enough,[121,122] is limited by high absorption requiring very small sample thicknesses[120,123] and therefore suffers from similar problems as electron diffraction.

Total scattering diffraction patterns for synchrotron XRD are captured on two-dimensional (2D) flat-panel area detectors (custom-build or purchased from commercial suppliers) that are capable of recording over a wide range of scattering angles θ or scattering vectors $\vec{Q}$ (modulus $Q = |\vec{Q}|$), respectively, simultaneously. This is possible since the used high energy E_i, i.e., small wavelength (Eq. (1)), "compresses" a wide Q-range into a cone (cf. Figure 7) with a small opening angle and enables the use of relatively compact setups.[11] No angular scan, as in laboratory XRD setups, is necessary, which would be impossible given the necessary high speed of the experiments anyway. Drawbacks of the method lie in the limited access to synchrotrons and time-consuming experiments. Especially in combination with CNL, the sufficient stabilisation of the sample can be challenging. The presence of the nozzle also prevents full visibility of the sample, rendering measurements of surface tension, viscosity, density or thermal expansion at least difficult. Possible future improvements will be discussed in Section 7.

In recent years, X-ray free-electron lasers (XFEL) have had their advent. Their pulsed nature allows monitoring very fast structural changes.[124–126] So far, XFELs have not been used to in-situ monitor vitrification but were, for instance, able to disclose LLCs in chalcogenide-based glasses.[125] The destructive nature of the intense X-ray pulses also demands novel ways of sample handling, which will be further discussed in the Outlook (Section 7).

Another challenge is the successive loss of information along the experimental route. During the diffraction experiment, the three-dimensional structure is reduced to information on a 2D detector and later reduced even more by azimuthal averaging to a one-dimensional function, the structure factor $S(Q)$. A partial reconstruction of the lost information would be possible by using different types of radiation, which is difficult as described above. To learn more about

the evolving element-specific local environments and chemical short-range order (CSRO) along the pathway other methods like computer simulations can be utilised. A relatively simple method is Reverse Monte-Carlo (RMC) refinement in which the position of the atoms in a simulation is varied until the structure factor coincides with the measured one.[127] From this final configuration, partial structure factors and all other information about local arrangement of the atoms, like bond lengths and bond angles, can be derived. The major drawback of this method is the massive overdeterminacy, i.e., a huge number of local configurations (three-dimensional) yield virtually identical structure factors (one-dimensional). Another computational method, molecular dynamics (MD) simulation, seeks to determine the structure based on solving the equations of motion for all atoms in a sample using interatomic potentials.[128,129] If these potentials are derived from first-principle quantum-mechanical calculations like density functional theory (DFT), the method is called ab-initio MD (AIMD).[130] The results of MD simulations can be used as additional input to improve RMC simulations. Currently, AIMD is too computationally expensive to be performed with the temperature increment as state-of-the-art diffraction experiments, but even a bigger step width can provide valuable insights.[45] DFT calculations can also be used to evaluate changes in bonding among atomic pairs along the pathway.

3. Structural functions

Incident monochromatic X-rays with energy E_i possess a wavelength

$$\lambda_i = \frac{hc}{E_i} \tag{1}$$

which translates to the modulus of the incident wave vector

$$\left|\vec{k}_i\right| = k_i = \frac{2\pi}{\lambda_i}, \tag{2}$$

where c is the speed of light in vacuum and h Planck's constant. Considering only elastic scattering the modulus $\left|\vec{k}_s\right| = k_s$ of the scattered wavevector is identical to that of the incident wavevector, i.e., $k_s = k_i$ or $\left|\vec{k}_s\right| = |\vec{k}_i|$ (Figure 7). The momentum transferred to the sample during the scattering event is expressed by the so-called scattering vector

$$\vec{Q} = \vec{k}_s - \vec{k}_i, \tag{3}$$

Of which, in the case of the isotropic nature (inset of Figure 7) of the amorphous material (liquid and glass), only the modulus $Q = \left|\vec{Q}\right|$ is of interest. Both vectors $\vec{k}_i$ and $\vec{k}_s$ are vectors in the so-called k -space (not Q-space) or *reciprocal space*. Instead of Q, in some publications q or K is used. The modulus of the scattering vector is related to the scattering angle 2θ (Figure 7), which is often used for presenting the results of laboratory X-ray experiments, by

$$Q = \frac{4\pi}{\lambda_i}\sin\theta. \tag{4}$$

The important quantity for structural analysis is $S(Q)$ the *total scattering structure function,* where 'total scattering' refers to the fact that the measured intensity comprises scattering not only from the atomic structure but also inelastic scattering due to the thermal movement of the atoms, i.e., their dynamics.[107] Ways of separating both exist by evaluating the so-called Debye-Waller factor.[131] For amorphous materials $S(Q)$ is usually referred to as the *structure factor,* which must not be confused with the crystallographic structure factor.[107] For all of the studies reviewed here, the Faber-Ziman formalism has been used.[107,132]

Although $S(Q)$ can already be used to analyse certain aspects of the structure, e.g., in connection with global electronic influences[133,134] and thermal expansion[49] more often information in *real space* (r-space) is desired, which can be obtained by a Fourier transform that yields the *reduced pair-distribution function*

$$G(r) = \frac{2}{\pi}\int_0^{Q_{max}} Q[S(Q)-1]\sin(Qr)\mathrm{d}Q. \tag{5}$$

$G(r)$ can be interpreted as the distribution of probability of finding the centre of another atom at distance r from an arbitrarily chosen atom (at $r = 0$) and can directly provide an insight into the typical shell structure of amorphous materials. If ρ_0, the material's (average) particle number density, is known further structural functions can be derived from $G(r)$ like the *pair-distribution function*

$$g(r) = \frac{G(r)}{4\pi\rho_0 r} + 1 \tag{6}$$

And the *pair density function* $\rho(r) = \rho_0 g(r)$. Both describe the shell structure as deviation from the mean density (of a structureless gas of the same mean density) to higher *as well as* to lower values. All these real-space functions give information on how the neighbourhood of an atom in the sample looks like on average. The *coordination number*

$$N_C = \int_{r_1}^{r_2} R(r)\mathrm{d}r, \tag{7}$$

Provides the number of atomic centres located between two concentric spheres with radii r_1 and r_2, where r_1 and r_2 usually delimit a nearest-neighbour (NN) shell. The function $R(r)$ in Eq. (7) is called *radial distribution function* (RDF) and can be calculated from $g(r)$ or $\rho(r)$, respectively, by

$$R(r) = 4\pi r^2 \rho_0 g(r). \tag{8}$$

Knowledge of the number density ρ_0, necessary to determine $g(r)$, $\rho(r)$, $R(r)$ and N_C, can be obtained by measuring the macroscopic mass density or, ideally, from the scattering data directly (the initial slope of $G(r)$ is proportional to ρ_0). However, the latter is prone to uncertainties along the chain of structure analysis. To determine the density macroscopically, the temperature-dependent volume of the sample needs to be known along the pathway, which, as already mentioned above, can be achieved by using cameras and appropriate lighting.[15,17,79] Unfortunately, especially for CNL, this method is less attractive as parts of the sample are hidden by the nozzle. It is therefore important to gain as much structural information from $S(Q)$ and $G(r)$ as the structural functions that do not depend on the knowledge of ρ_0. Throughout this review, we use the term *structural function* for the functions in reciprocal as well as in real space. It must not be confused with the term *structure function*.

4. Data acquisition and reduction

Temperature-dependent measurements upon cooling result in a huge amount of data depending on the temporal as well as spatial resolution of the detector. From the scattered intensity captured as diffraction patterns on the area detectors (Figures 6 and inset of 7) to the structural functions in real space, many steps are necessary, which are carried out using several specialised software packages. Some of them are specific to a particular setup (mainly at early steps in the toolchain of data analysis) or common for a facility, beamline or particular research group. Others, like those to perform the Fourier transform, can be used interchangeably.

The raw data is influenced by several factors not intrinsic to the measured material. These are related to the X-ray source, the sample environment, as well as the detector and need to be corrected for.[11,107] Routines for these corrections are usually included in the corresponding software packages.

Diffraction patterns of amorphous materials are characterised by diffuse concentric rings (halos). Using e.g., DAWN[135,136] or FIT2D,[137] the diffraction patterns are azimuthally integrated to obtain the integrated diffraction intensities $I(Q)$. With subsequent normalisation to the X-ray atomic form factor and conversion to electron units per atom (generalised Krogh-Moe-Norman method[138,139]) the total structure factors $S(Q)$ can be calculated. Dedicated software for this step is e.g. GudrunX[140] or PDFgetX3 [143] which also Fourier transforms $S(Q)$ to the reduced pair-distribution function $G(r)$ as outlined above. While ideally Q_{max} in Eq. (5) is infinite, in practice it is necessary to choose a finite value, usually as high as possible, depending on the raw data. Improper choice can introduce artifacts in form of additional oscillations in $G(r)$ ("termination ripples"), which can be somewhat mitigated by the use of modification functions during Fourier transform.[141] PDFgetX3 has been developed as a rapid and highly automatable software that can readily process hundreds of X-ray diffraction patterns within a few seconds[142] and is thus especially useful for the high number of temperature-dependent diffraction patterns taken along the pathway. In the end, a variety of plotting programs can be used to visualise, e.g., the temperature-dependent structural functions $S(Q,T)$, $G(r,T)$, $R(r,T)$.

For the mentioned RMC calculations, also a variety of software packages are available, with RMCProfile[143] and RMC++[144] being the most common. MD simulations are most commonly carried out based on the LAMMPS code.[129] For DFT calculations, the SIESTA code[145–147] is often used, which employs the standard Kohn-Sham self-consistent scheme in local density approximation (LDA).

5. Data analysis

The two main results that can be obtained (more or less) directly from the in-situ measurements are the cooling curves $T(t)$ and (after the corrections outlined in Section 4) $S(Q)$, i.e., $S(Q,T)$ to be precise. All other structural functions are in turn derived from $S(Q,T)$. Although the main aspect of this thesis is the evolving structure, the cooling curves $T(t)$ themselves yield important results beyond indicating the sample temperature during cooling. From $T(t)$ the temperature rate $\dot{T}(t)$ can be calculated (upon cooling its values are negative; the absolute value is then called "cooling

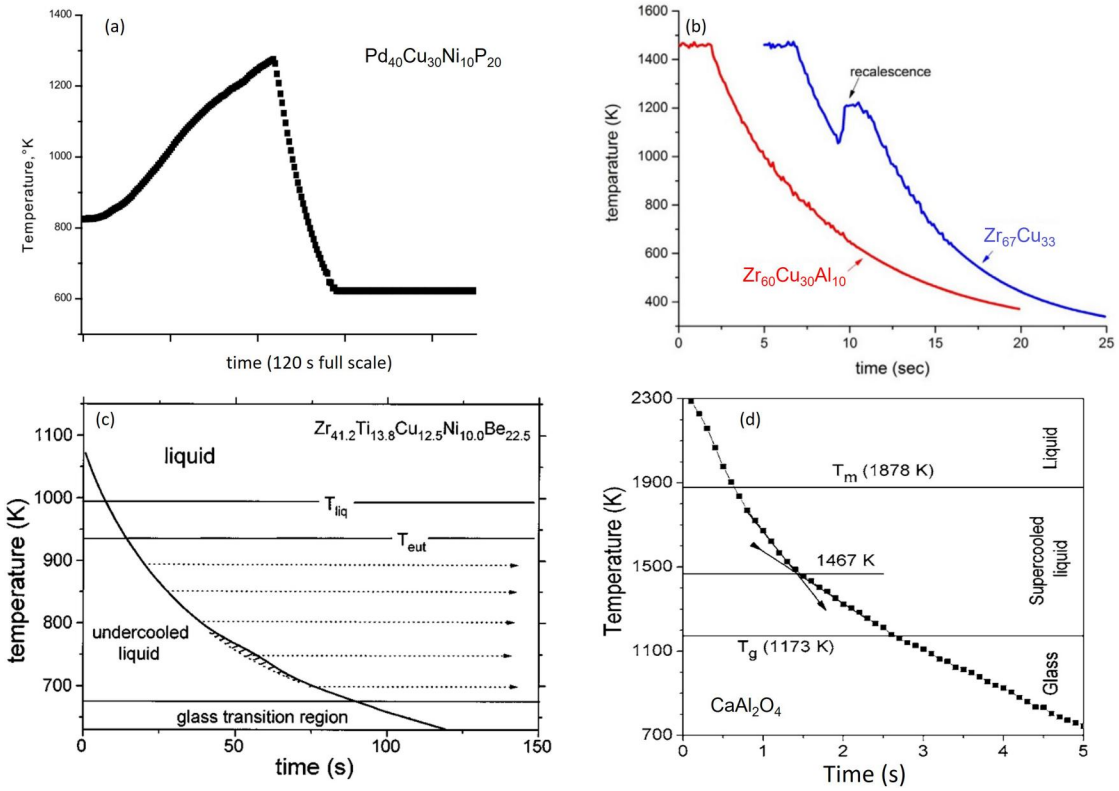


Figure 8. Examples of several $T(t)$ functions ("cooling curves") and proposed interpretations. (a) The first reported in-situ vitrification ($Pd_{40}Cu_{30}Ni_{10}P_{20}$) showing no recalescence that would point to crystallisation during free cooling after switching off the sample heating (reproduced with permission from ref. [33]). (b) The comparison of $Zr_{60}Cu_{30}Al_{10}$ and $Zr_{67}Cu_{33}$ shows that in-situ vitrification of the latter alloy could not be achieved due to the intervention of crystallisation evidenced by the recalescence event at about 1050 K (this also shows the beneficial effect of Al on GFA) (reproduced with permission from ref. [45]) (c) In $Zr_{41.2}Ti_{13.8}Cu_{12.5}Ni_{10.0}Be_{22.5}$ a small recalescence event (hatched area) was attributed to a decomposition of the undercooled liquid with respect to Zr and Be (reproduced with permission from ref. [148]). (d) A possible kink (determined using two tangents) in the cooling curve of $CaAl_2O_4$ interpreted as an increase in the degree of order related to a dynamical crossover temperature causing changes in thermodynamic properties as well (reproduced with permission from ref. [19]).

rate"). Upon free cooling, i.e., after deactivating all heating equipment, $\dot{T}(t)$ strongly changes (Figure 8), and an exponentially decaying temperature is expected.

Knowledge of $\dot{T}(t)$ is important in comparing different experiments and materials since effects like LLCs may be temperature-dependent (Section 6.2). Major deviations occur if the sample crystallises and recalescence occurs, which leads to sharp temperature increase due to the release of latent heat of crystallisation. This behaviour is, of course, not desired as it prevents vitrification. Whether the glass transition can be observed by a small kink in $T(t)$ at T_g is not always, clear although it has been reported.[39] For an oxide-glass-forming liquid, a small kink in $T(t)$ related to a possible LLC has been reported[19] as well as the visibility of decomposition of a Zr-based metallic glass.[148] With the knowledge of the emissivity of the material and the Stefan-Boltzmann law, the temperature-dependent specific heat $c_p(T)$ of the alloy can be determined.[18,80]

Deeper insights can be gained by closer scrutiny of the details of the structural functions. Since in both reciprocal and in real space these functions consist of a series of peaks (and troughs, i.e., "anti-peaks") it is fruitful to analyse those and their temperature dependence independently. Quantities like positions, widths or heights of peaks are commonly called *structural metrics* and can be obtained by different methods as will be discussed further down. Great care must be taken when ascribing a physical meaning to a peak and according metrics. Furthermore, there is no unique and agreed-upon procedure for how the structural functions can be "dissected" into those peaks (halos for $S(Q)$ and NN shells for $G(r)$) nor where a peak begins/ends or if some sort of background needs to be subtracted[149] (Figure 9). However, the choice of background is subjective and may lack physical

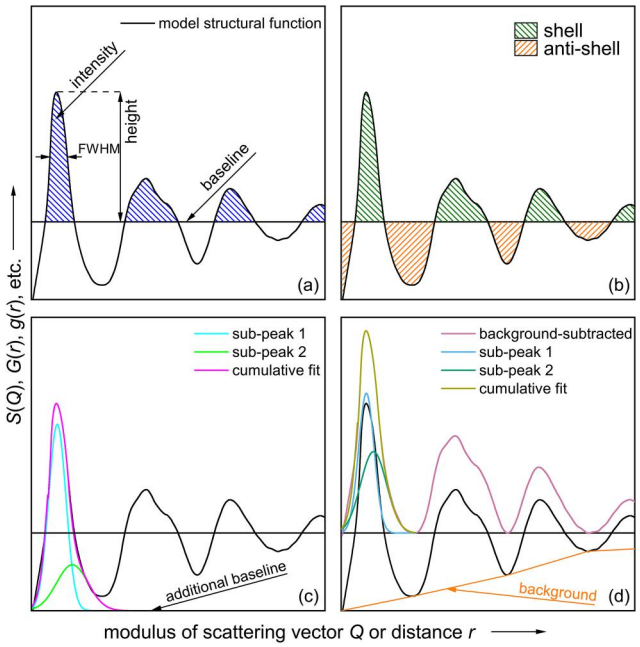


Figure 9. Possible ways of extracting peaks from a model structural function (black) and their fitting: (a) using the parts above a baseline, implied by the average of a structural function, (horizontal black line) only (peaks not necessarily to be fitted), (b) using portions above and below that baseline (especially in real space called NN shell and anti-shell), (c) defining an additional baseline for a fit (shown exemplarily for the first peak fitted by two sub-peaks), (d) removing a background (orange, determined by a set of linear functions) before fitting. In a) the definitions of intensity, height and FWHM are highlighted.

justification. One form of background is constructed by connecting the minima of the functions *via* straight lines.[42,149] This method misses important temperature-induced structural changes in the troughs between the peaks, i.e., it would cause a peak to increase in height although actually the adjacent minima get deeper with decreasing temperature.[42] Given that the structural functions oscillate about a line of constant y (e.g., $S(Q) = 1$; $G(r) = 0$; $g(r) = 1$) using the intersections of these functions with that line can be used to demarcate the peaks.[150] Alternatively, the local minima within the troughs (or zeros after background subtraction) can be used (Figure 9c,d). For results of simulations, a less arbitrary way has been proposed in the case of $R(r)$.[151,152] Different kinds of functions are commonly fitted to the individual peaks before they are subject to further analysis. Fits are performed for different reasons: (i) smoothing out noise from the experiment, where the type of functions and number of curves fitted to one peak can be chosen arbitrarily (depending on time and computational power available), since no physical meaning is attached to the functions and the only aim is to reproduce the experimental curve as well as possible with scatter removed, (ii) showing that the peak consists of two (or more) features (by fitting two or more curves) that, e.g., may behave differently depending on temperature (e.g., first NN shell in ref.[45]) or (iii) fitting of two or more curves, especially in r -space, that are supposed to directly relate to expected partial pair correlations or bond lengths of elemental pairs in the alloy. The latter has to be done with great care and is often ill-fated when too many components are present. Even with less components, although tempting, sub-peaks do not automatically relate to certain elemental pairs of the same number. The used fit functions depend on the authors and the purpose of the fit. Gaussian functions are frequently used,[42,45,149,153] but also Lorentzian functions or combinations/convolutions of both in the form of Voigt or pseudo-Voigt functions[40,56,154]), as well as spline functions.[17,18,44,57,64] Using different fit functions to obtain different parameters from a peak has been used as well.[17]

From the individual peaks or their fitted version, several parameters or characteristics can then be derived and analysed as well as plotted as temperature-dependent structural metrics. The peak position may be considered the most straightforward, although the position of the maximum (i.e., the x -value belonging to the highest y value), the position of the centroid (centre of mass, i.e., first moment) or a quantity called R_{50}[42] (the x -value for which 50% of the peak area is below as well as above) can be meant, where authors do not always clearly indicate which definition they followed or if a baseline correction was carried out, which can impede comparability of results. Subsequently, other metrics suffer from the same issue. For the width of a peak, often the full width at half maximum (FWHM) Γ is used, but its second moment (i.e. variance)[43] may deliver comparable information with less scatter. Further commonly used metrics are height of the peak or area of the peak, where peak area, rather than its height, is linked to its intensity. Also, the skewness or asymmetry of a peak can be analysed following different definitions, e.g., by comparing the left and right half-width,[155] the relative positions of the maximum and the centroid, or by calculating its third moment. In general, metrics that involve an integration (centroid and other moments) are much more robust since they naturally include an averaging over many values. Frequently ratios of different metrics are discussed as well.[42,75,149,154] Calculating and analyzing the moments removes the subjectivity of choosing a specific fit function[43,156] and in principle also moments beyond the third one can be used to

discern possible temperature-dependent changes in behaviour (e.g., related to a possible LLC) along the pathway, although the physical meaning may not always be straightforward. The aforementioned quantities are sometimes taken only from sub-peaks or shoulders after applying fitting procedures.[43] Although highlighting those temperature-dependent changes is usually the intention behind an author's selection of a specific structural metric, due to the constraints of the experiment, one metric may have less noise than another and is therefore preferred.[17] Calculating the relative Gaussian and Lorentzian proportion of a fitted Voigt profile was proposed as another way of gaining further structural insights.[154] By using the intersections of the structural functions with their respective baselines to define peaks[17,45,55,57] and their analysis in terms of moment-related metrics without any fitting can be considered the least subjective processing. This procedure inspired the "shell/anti-shell" concept, which was shown to yield better-defined metrics with less scatter.[150] Generalised to include metrics in reciprocal space as well ("halo/anti-halo") this method could be referred to as "peak/anti-peak" concept, with "anti-peak" being the troughs in the structural functions. One of the assets of the "shell/anti-shell" concept is its recognition that structure, especially in real space, means deviations from the mean density to higher as well as to lower local density while not preferring the former over the latter. Additionally, the "shell/anti-shell" concept removes spurious increases in peak heights, which are actually caused by deepening troughs, and decreases the influence of subjectivity even further. Analyzing the temperature dependence of the anti-peaks, an additional set of metrics providing valuable information about the structural evolution along the pathway can be obtained.

6. The pathway

An experiment for in-situ monitoring the pathway should be designed to commence at a temperature sufficiently higher than the alloy's T_l, ideally with the sample even overheated to several hundred kelvin above T_A, the temperature that marks the onset of cooperative re-organisation of atoms and the beginning of glass formation in the liquid alloy.[9] From the overheated condition, after passing milestones like possible (maybe even mandatory) LLCs, vitrification takes place and yields an amorphous solid called a glass. Structure and properties of the latter are not unique but depend on the overheating as well as the cooling rate.[157,158] When the alloy stays liquid below its T_l it is referred to as undercooled liquid (UCL). The frequently used term "supercooled" is assumed here to be synonymous with "undercooled" but may be somewhat misleading since "super" has the meaning of above, not below.

Figure 10a exemplarily shows $S(Q,T)$ for $Zr_{60}Cu_{30}Al_{10}$[45] along the pathway in a three-dimensional way using a so-called "waterfall plot."[33,37,45,153] The same information can be illustrated in a contour plot (Figure 10b). After Fourier transform, all real-space structural functions, most importantly $G(r)$, can be visualised in the same way. Figure 10c shows the corresponding reduced pair-distribution functions $G(r,T)$ for $Zr_{60}Cu_{30}Al_{10}$[45] as a 2D projection where T -dependent trends can be followed with the help of an appropriate color scale. All these T -dependent plots can be supplemented by movies showing the structural evolution in about the real experimental time.[46]

In the following, a closer look will be taken at the milestones along the pathway and how they may show in structural data gathered by in-situ high-energy synchrotron X-ray diffraction experiments. Paralleling the experiment, the discussion starts at high temperatures and follows the pathway towards lower temperatures.

6.1. Undercooling

After the alloy has successfully passed the first step of the pathway towards vitrification by entering the UCL regime, structural changes at the atomic scale that finally lead to vitrification could now be identified. Contrary to experiments investigating the structural changes of metallic glasses on heating or during isothermal holds,[34,35,47–53,159–161] respectively, rapid cooling experiments have the potential to continuously probe the sample in an amorphous regime down to T_g and enable the determination of the functional relations of the T-dependence of structural metrics. The intervention of crystallisation prevented the latter during the experiments in heating or at isothermal holds. Due to initial limitations of detector speed, the density of data points of the early studies on cooling that achieved in-situ vitrification was low, and details of the functional dependence still could not be resolved yet.[33,149,153] Qu et al. were the first to publish quasi-continuous sets of structural data over a wide temperature range along the pathway in the form of the position of the principal maximum in the diffraction intensity $I(Q,T)$.[40] Despite the relatively strong scatter, a non-linear behaviour became visible for temperatures above T_g in Zr-based metallic glasses

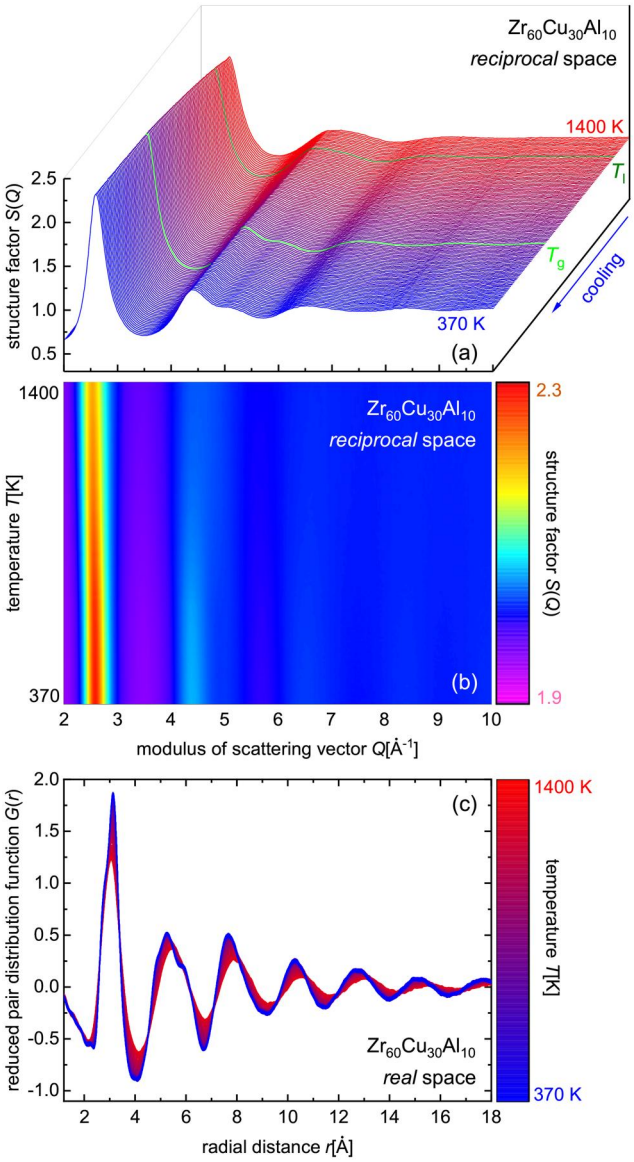


Figure 10. The evolution of structural functions along the pathway exemplarily for $Zr_{60}Cu_{30}Al_{10}$ during cooling from 1400 K (red) to 370 K (blue) (data taken from ref. [45]). This also showcases different ways of visualising structural functions along the pathway. In (a) the T-dependence of the structure factor $S(Q,T)$ is shown in a three-dimensional way as waterfall plot. Highlighted in green are the functions for the liquidus temperature $T_l = 671$ K and the glass-transition temperature $T_l = 1207$ K. Alternatively, in (b) the T-dependence of the structure factor $S(Q,T)$ is shown as contour plot. The corresponding reduced pair-distribution functions $G(r,T)$ are shown in (c) as 2D plot. Here T-dependent trends in the in the large amount of data can be followed with the help of the color coding.

(Table 1). Data with a high density of data points and at the same time a much higher signal-to-noise ratio was presented by Georgarakis et al.[45] for $Zr_{60}Cu_{30}Al_{10}$, including the additional step to obtain $S(Q,T)$ from $I(Q,T)$ (Section 5). Of $S(Q,T)$ the position $Q_1(T)$ of the principal peak as well as its height $S(Q_1,T)$ was analysed, showing the non-linear temperature-dependence above T_g much clearer (Figure 11). Recently, Ryu et al. demonstrated the curvature of $S(Q_1,T)$ with high clarity for $Pd_{42.5}Cu_{30}Ni_{7.5}P_{20}$.[37] The latter study showed that a Curie-Weiss-like function, originally known from the description of magnetic ordering phenomena,[162] can be fitted to $S(Q_1,T)-1$ with a negative characteristic temperature (quasi-Curie temperature) that has been associated with a proposed hypothetical "ideal-glass state" that possesses long-range (non-decaying) density correlations.[37,154] In MD simulations for several other metals (elements and alloys), a comparable behaviour could be observed.[37] Further experimental studies have to validate the generality of this behaviour, but it seems to be more common than expected (exemplified by the red dashed curve for $Ni_{62}Nb_{38}$ in Figure 11). Compared to $S(Q_1,T)$ the non-linear behaviour for $Q_1(T)$ is less pronounced.[17,18,35,40,45,47,50,163] In any case, the presence of curvature casts doubt on results derived from fitting linear functions or tangents to temperature-dependent structural metrics, especially since their slope depends on the T-range they are fitted to.[35,45,50,64,159,160,164] The latter is either strongly influenced by subjectivity or insufficiently known due to experimental constraints (accessible T -range).

A curvature (Figure 11) with increasing (negative) slope upon cooling indicates an acceleration of the structural evolution upon increasing undercooling.[43,45,159–161] Anomalies in the way this acceleration takes place may be related to LLCs (Section 6.2) reflecting changes in fragility. In real space, non-linear changes of structural metrics with temperature were observed as well,[17,18,35,43,45,50] probably related to the same effects as in reciprocal space, showing that the accelerated ordering spans various length scales belonging to short- (SRO) as well as medium-range order (MRO).

MD simulation data accompanying the experimental results suggest that during progressing undercooling, more and more atoms are gathered in clusters.[43,45,165–167] This enhancement of the SRO is often predominantly characterised by icosahedral-like symmetry with strong covalent bonding (hybridisation effects).[45,165–167] The number of icosahedral-like clusters shows a non-linear behaviour comparable to the metrics discussed above, highlighting again the accelerated structural evolution in the UCL corroborating the finding in reciprocal space mentioned above (Figure 12). Icosahedral SRO is associated with the stabilisation

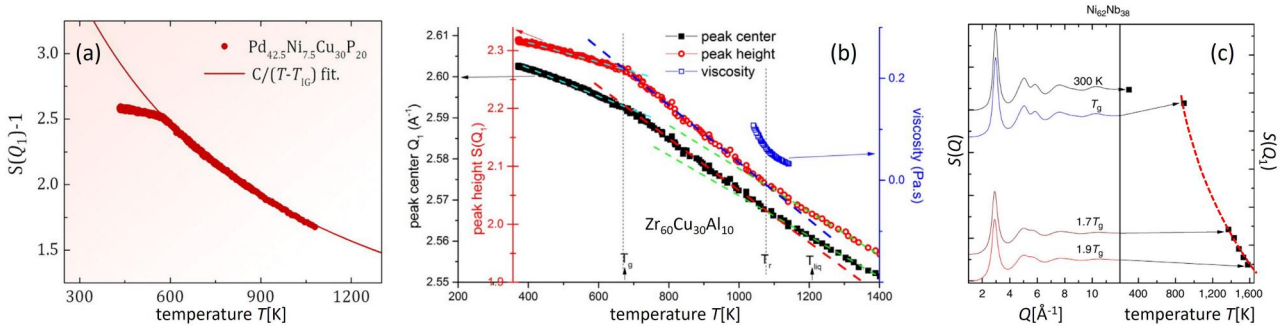


Figure 11. Non-linear temperature dependence of structural metrics in reciprocal space for different metallic glasses. A Curie-Weiss-like behaviour has been proposed recently and was fitted to the experimentally obtained height $S(Q_1) - 1$ of the first peak of the structure factor of $Pd_{42.5}Cu_{30}Ni_{7.5}P_{20}$ (a, reproduced from ref. [37]). For the height $S(Q_1)$ and position Q_1 of $Zr_{60}Cu_{30}Al_{10}$ the continuous non-linear shape has been approximated discontinuously using two linear functions each whose intersection was associated with a stark increase in the viscosity $\eta(T)$ (b, reproduced with permission from ref. [45]). A lack of data for wide T regions severely hampers a correct fit as in the case of $Ni_{62}Nb_{38}$ (c, adapted with permission from ref. [161]) but again allows for a non-linear dependence over the complete T region down to T_g as sketched by the red dashed line while originally a linear approximation[161] was used for the high-T region only.

of the amorphous structure against nucleation of crystalline phases[173] and the covalent bonding character to a shortening of interatomic distances or increased packing efficiency.[45,149,174,175] Both aid the significant slowing-down of the relaxation kinetics related to the sharp increase in viscosity towards vitrifaction.[149,176] Experiments also revealed that the first NN shell seems to exhibit negative thermal expansion.[35,45,51,153,177] After demonstrating this clearly for $Pd_{40}Cu_{30}Ni_{10}P_{20}$ upon cooling by Georgarakis et al.[153] the same behaviour has been reported numerous times for other alloys as well.[18,45,177] Further results showed that this effect is not limited to alloys but even occurs in liquid elements.[178] An explanation was given in terms of the developing clusters along the pathway. At high temperatures only the strongest bonds survive, and clusters are relatively small, i.e., the coordination number N_c is low. The developing bonds on cooling cause more atoms to enter the clusters, causing their radius (roughly the first NN distance) as well as N_c to increase.[153,178] At the same time the packing density increases which, in turn, is beneficial for high GFA.[176] This behaviour stops abruptly at T_g highlighting that it is caused by structural changes in the UCL and not a"real" negative expansion.[46] All higher NN shells exhibit a positive expansion[35,177] with NN shells two and three expanding even stronger than observed macroscopically.[46] This illustrates that it is the MRO that determines the macroscopic thermal expansion. Since MRO also determines the position of Q_1 in $S(Q)$[154,179] highlights the importance of the Yavari equation[34,49] for the description of thermal expansion. Since atoms located on NN shells belonging to the MRO are at the centre of their own SRO, both should be describable on common grounds. However, the MRO seems to be governed by its own emergent many-body effects.[46,154,180] Global electronic interactions have been invoked to describe the characteristic distances of the MRO.[46,133,134,150,181] It remains to be seen if such a global description will be able to aid a deeper understanding of glass formation and glass transition. Interestingly, during undercooling it is not only the clusters constituting the first NN shell that "absorb" atoms, but it could be shown quite generally that atoms are transferred from anti-shells to shells (Figure 13) which can be interpreted as a signature of increasing structural order along the pathway.[45,46,150]

Apart from analyzing distances, other real-space metrics have been used to underline the structural changes during undercooling and their relationship with the slowdown of kinetics.[42,149] The evolution of clusters and their interconnection changes the activation energy for viscous flow. In this respect, the intensity ratio of two sub-peaks, fitted to describe the first NN shell for $Pd_{40}Cu_{30}Ni_{10}P_{20}$[36] and $Zr_{55}Cu_{30}Ni_5Al_{10}$,[42] has been considered. Not only is this metric showing the accelerated evolution again, but their curved T -dependence parallels that $\eta(T)$ for $Pd_{40}Cu_{30}Ni_{10}P_{20}$ remarkably well.[149] This was interpreted as the CSRO providing the structural basis for the stark increase of $\eta(T)$ in the UCL region towards vitrifaction.[149] Comparing the evolution of the intensity ratio for both $Pd_{40}Cu_{30}Ni_{10}P_{20}$ and $Zr_{60}Cu_{30}Al_{10}$ a relation to fragility seems to be encoded in this metrics;[42,149] the stronger the structural changes upon cooling, the more fragile the alloy is. Further attempts to find structural signatures for fragility have been made by constructing metrics that are able to

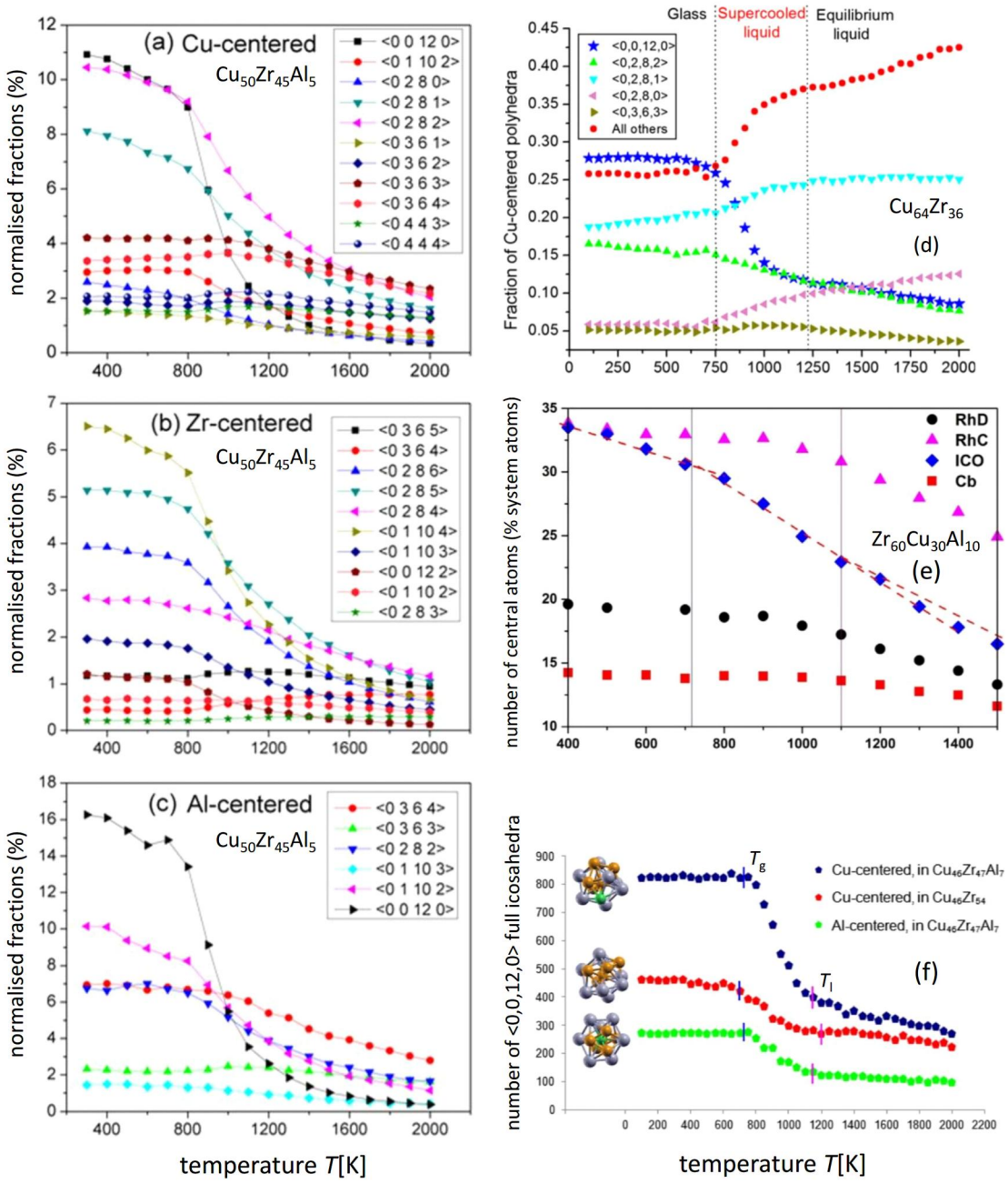


Figure 12. Results from MD simulations of various metallic glass forming liquids upon cooling. A rapid acceleration of cluster formation in the undercooled regime is clearly visible. This is especially the case for clusters with icosahedral-like symmetry. In (a), (b), (c), (d) and (f) so called Voronoi indices[168,169] are given where <0,0,12,0> relates to perfect icosahedral symmetry, i.e. central atoms enclosed by Voronoi polyhedra (VP) with 12 pentagonal faces. (a–c) Shows the cluster evolution around the different elemental species in $Cu_{50}Zr_{45}Al_5$ (reproduced with permission from ref. [170]). For $Cu_{64}Zr_{36}$ the growth of the <0,0,12,0> VP on the expense of clusters with other symmetries is highlighted in (d, reproduced with permission from ref. [171,172]). In (e) cluster populations with rhombic dodecahedral (RhD), icosahedral (ICO) and cuboctahedral (Cb) shapes as well as the sum of the population of RhD and Cb clusters (RhC) are shown for $Zr_{60}Cu_{30}Al_{10}$ (reproduced with permission from ref. [45]). A comparison of the population of <0,0,12,0> clusters in $Cu_{46}Zr_{47}Al_7$ and $Cu_{46}Zr_{54}$ is shown in (f, reproduced with permission from ref. [165]). As in the experimentally obtained metrics (Figure 11) mainly continuous non-linear dependences of the populations between T_l and T_g are visible.

emphasise small details. Additionally to the findings of Louzguine et al.,[42,149] it could be shown that fragility is connected to the structural evolution in the MRO on distances around the fourth NN shell.[18,44] In the following signatures of structural crossovers, maybe related to changes in fragility, are discussed.

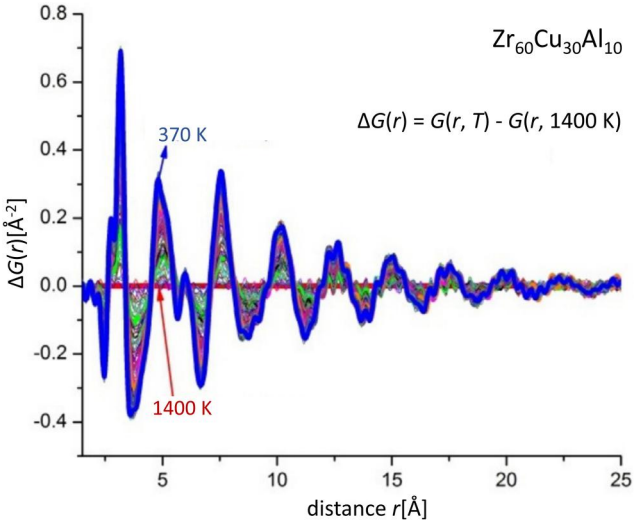


Figure 13. The function $\Delta G(r,T) = G(r,T) - G(r,1400)$ K for $Zr_{60}Cu_{30}Al_{10}$ shows the transfer of atoms from the anti-shells to the shells upon undercooling, i.e., an increasing height of the peaks of $\Delta G(r,T)$ accompanied by a decreasing depth of the throughs (reproduced with permission from ref. [45]).

6.2. Liquid-liquid crossovers

The experiments that were able to monitor the vitrification *in situ* (Table 1) show changes in slope, frequently called "kinks" (Figure 11), in several structural metrics, which are ascribed to the glass transition at T_g (Section 6.3). However, additional anomalies along the pathway were reported by several authors. To get reliable results, data for a temperature range as wide as possible is necessary, which is not always provided. Even if a putative kink is close to the centre of the measured temperature interval, its determination is not always without doubt. Sometimes kinks are identified with the help of "tangents" (Figure 11).

However, this approach is somewhat subjective and may cause the detection of transitions or crossovers where there may actually be none.[43,45] Step-like "double-kinks" were found in the temperature-dependent position $Q_1(T)$ of the first maxima of Zr-based alloys (Vitreloy 1 and 106a).[17,18,163] The associated change in behaviour takes place over relatively small temperature intervals and was ascribed to LLCs (Figure 14). Interestingly, these step-like kinks can point "downstairs" (Figure 14a) or "upstairs" (Figure 14b) where no explanation for the different direction was reported.[163] Difficulties in interpretation may arise from the evolution of the different partial structure factors of these multi-component alloys during the LLC which cannot be disentangled easily.[163] The macroscopic density remains virtually unchanged across the LLC in Vitreloy 1 and 106a, and the slow transition

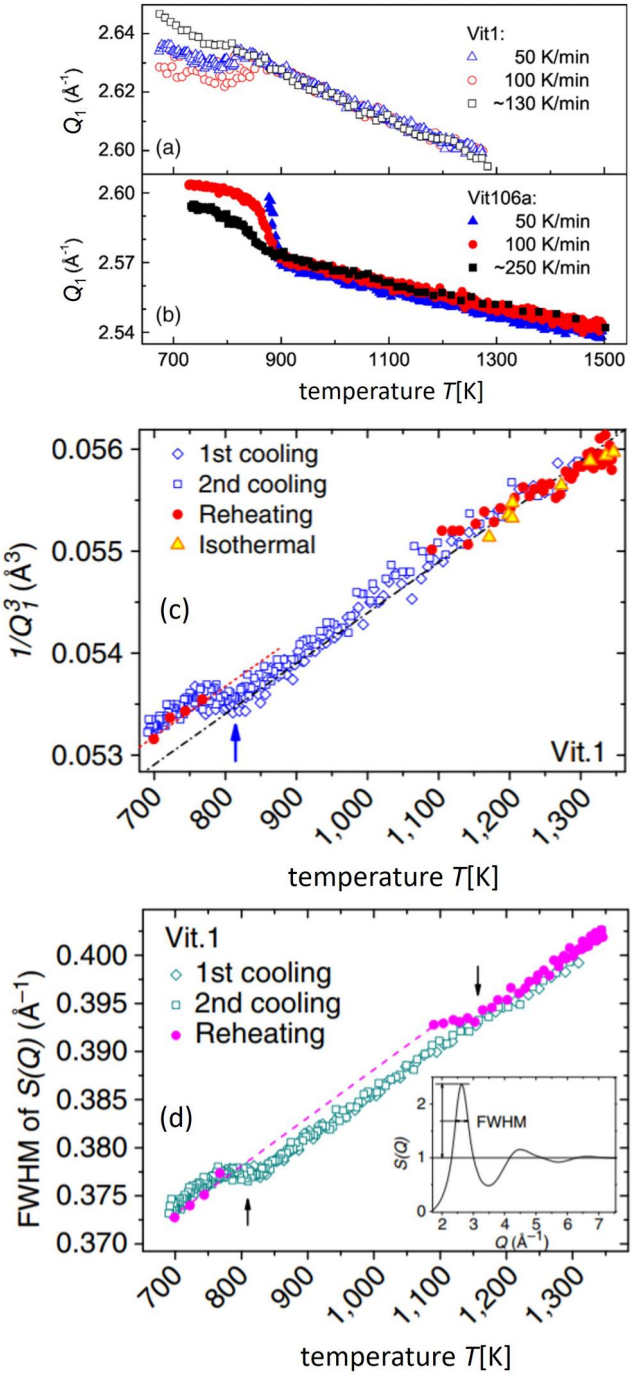


Figure 14. Kinks in structural metrics in reciprocal space during supposed LLCs and their temperature dependence. (a) The position Q_1 of the first peak of $S(Q)$ of Vitreloy 1 ($Zr_{41.2}Ti_{13.8}Cu_{12.5}Ni_{10}Be_{22.5}$) for three different cooling rates (reproduced with permission from ref. [163]). (b) the same for Vitreloy 106a ($Zr_{58.5}Cu_{15.6}Ni_{12.8}Al_{10.3}Nb_{2.8}$) (reproduced with permission from ref. [163]) (c) $1/Q_1^3$ (which is supposed to be a microscopic measure (esp. MRO) of the volume of the alloy) for Vitreloy 1 (reproduced with permission from ref. [17]) (d) FWHM $\Gamma(T)$ of the first peak of $S(Q)$ of Vitreloy 1 showing indications (marked by arrows) of a hysteresis (reproduced with permission from ref. [17]).

kinetics was found incompatible with only local structural changes.[17,18,163] Additionally, a strong cooling rate dependence was found (Figure 14a,b). The higher

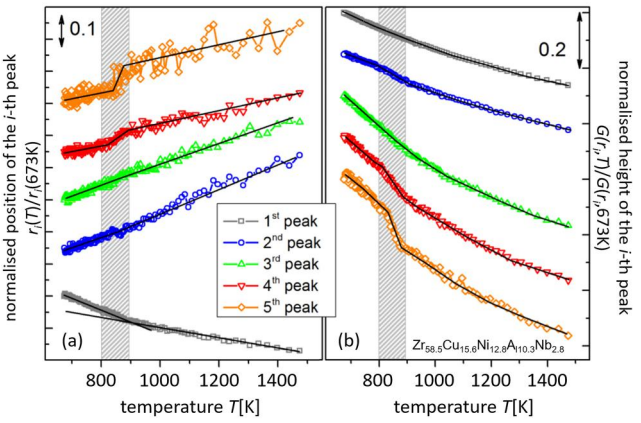


Figure 15. Kinks in the normalised position $r_i(T)/r_i(673\ K)$ and height $G(r_i,T)/G(r_i,673\ K)$ of the first five peaks ($i = 1...5$) during an LLC (hatched region) of Vitreloy 106a ($Zr_{58.5}Cu_{15.6}Ni_{12.8}Al_{10.3}Nb_{2.8}$) upon cooling (reproduced with permission from ref. [18]) Curves are shifted on the *y*-axes for clarity and the solid lines are a guides to the eyes. Note the combined occurrence of kinks and non-linear behaviour.

the cooling rate, the less pronounced the kinks are.[163] While the results shown in Figure 14 were taken by an ESL setup[17,18,163] CNL was used for $Zr_{60}Cu_{30}Al_{10}$ (Figure 11). Given the about 50 times higher cooling rates for the latter (Table 1) and the trend observed in ref. [163] (Figure 11a,b) LLCs may almost be invisible in CNL experiments without elaborate data treatment (possible ways of enhancing the visibility of LLCs in structural metrics have been proposed, cf., e.g., refs. [13,45]). To clarify this important issue, alloys with pronounced kinks found in ESL would need to be investigated in a CNL setup additionally. For $Zr_{41.2}Ti_{13.8}Cu_{12.5}Ni_{10}Be_{22.5}$ (in $\Gamma(T)$) in addition to a kink at lower temperature during cooling, a similar kink at higher temperature on heating was reported (Figure 11d), which was taken as an indication of a hysteresis.[17] However, the lack of data for the sample possessing a fully amorphous structure during heating between T_X and T_l makes the clear identification of the hysteresis difficult. Further investigations are necessary to see whether a hysteresis can be seen in other (structural) metrics and other alloys as well. Indications for the latter were recently reported.[182] Furthermore, it is not clear whether T_{LLC} it depends on the cooling rate.[163] The existence of both non-linear behaviour and kinks in the same alloy (Figure 15) highlights that the accelerated evolution probably is the "normal" behaviour and LLCs are occurring additionally under certain circumstances. Finally, a possible LLC may be bypassed completely during rapid undercooling (path b in Figure 1a), not unlike possible crystalline phases[61,183,184] and will be visible only upon heating the vitrified sample. Such a behaviour would bear similarities with recent reports of a possible "glacial-glass phase" in metallic alloys.[184]

To increase the confidence for a surmised LLC, it should be reflected in nonstructural quantities as well. Such quantities can, for instance, be the temperature-dependent viscosity $\eta(T)$,[45] density (back projection of the levitating drop)[17] or thermodynamic properties like the specific heat.[18] Anomalies in the specific heat have been shown, which were discussed in relation to a possible first-order nature of LLCs.[17,18,32] However, this is not readily observed in the cooling curves $T(t)$ for metallic glasses[18,45] (a possible kink in $T(t)$ was reported for oxide glasses, though).[19] Viscosity, on the other hand, is virtually never known over the complete T -range of the pathway, since the huge change in its magnitude cannot be measured with a single method.

The proposed origins of LLCs are probably diverse and also controversial. However, an LLC should originate in intrinsic structural changes. Competing explanations have been put forward as well as attempts for a unified description.[31,32,185] That the aforementioned kinks in the structural metrics can "bend" in both directions[163] makes it even harder to determine the underlying reason and hints at possibly different reasons and underlying mechanisms for LLCs. With respect to the opposite evolution of distances for the first NN shell compared to that of the higher NN shells, as discussed above (Section 6.1), it could be possible that at some T the clusters approach a critical size, triggering a reconfiguration on the length scale of the MRO during the LLC.[17] Such changes at the level of the SRO are related to an increased number density and packing efficiency of locally preferred clusters.[18,45,186] Furthermore, clusters increasingly tend to form backbones (MRO correlations) during undercooling, which are going to percolate the sample at a specific temperature, which may be related to T_{LLC}.[43,186–188] These backbones may be interpreted as partial solidification of the sample.[43] Using MD simulations of $Cu_{64}Zr_{36}$ this percolation was found to take place at about $1.4T_g$ and is also related to the onset of glassy dynamics.[186] Since percolation affects the dynamical properties, LLCs are often associated with fragile-to-strong transitions or crossovers (FSC).[25,26] Backbone formation has been connected to the onset of glassy dynamics[186,187,189] making LLCs maybe precursors, or even necessary prerequisites, for vitrification. With energy barriers lower than for the liquid-crystal transformation[17] LLCs may be likened to Ostwald steps;[31,190,191] however, not necessarily towards a crystal but towards a

glass. The (possibly kinetically stronger) liquid below T_{LLC} can resist crystallisation better, which may be key to increased undercoolability[17] and eventually high GFA.

Since T_{LLC} is often close to the critical temperature $T_C \approx 1.25T_g$ of the mode-coupling theory (MCT)[43,192] it is tempting to identify both temperatures,[43] but only the temperatures being close is not sufficient to make this assertion without further validation,[43] if MCT is applicable for metallic glasses at all.[193] Nevertheless, it is not unreasonable that a connection between the dynamical crossover of the MCT or similar theories and a crossover observable in structural metrics exists. It remains to be seen how close developing backbones,[186,188,189,194] collectively moving atoms in MCT[192] or so-called cooperatively rearranging regions[195,196] of the Adam-Gibbs description of the relaxation dynamics in undercooled liquids[195] are related. The ratio T_{LLC}/T_g may not be fixed for all classes of metallic liquids, and LLCs may even occur above T_l, multiple transitions may appear at different T in the same undercooled liquid[32,187] and an LLC may even be in competition with vitrification.[57]

Possible chemical decomposition involving long-range mass transport[163] or nanoscale demixing into different liquids, as surmised in oxide glasses, has also been put forward in connection to LLCs.[85] Temperature-dependent changes in the electronic structure have been proposed too.[182]

The increasing cooperativity during cooling begins with atoms forming clusters or associates in the equilibrium liquid way above T_l and leads to the aforementioned formation of percolating backbones.[186,188,189,194,197] In a sense, the connection of clusters to backbones can be seen in analogy to the formation of polymers from monomers and the formation of the monomers from single atoms. A polymer has to be considered a different material than the individual monomers from which it emerges. In this respect, the interpretation of fragile-to-strong crossovers can be seen as a chemical transition. It is not a single material showing a change in the temperature dependence of the viscosity, but a mixture of the polymer as well as remaining monomers and individual atoms, where more and more polymer with $\eta(T)$ different properties from that of the monomers is created upon cooling. Following this view, it needs to be investigated why polymerisation preferably takes place at the observed T_{LLC} and how close the relationship to "traditional" polymers is.

Recently, the transition to a "glacial-glass" was surmised to take place *via* a first-order LLC in the UCL regime of $La_{32.5}Ce_{32.5}Co_{25}Al_{10}$ on heating.[184] Similar indications can also be seen for $Ti_{40}Cu_{34}Pd_{14}Zr_{10}Sn_2$[61,198,199] and $Pd_{42.5}Ni_{42.5}P_{15}$,[200] where in the latter the new state was entered by varying the conditions of the high-temperature melt before quenching. Other recent observation, may fall under this scope as well.[201–204] It is, however, not yet clear whether the "glacial-glass" is really of amorphous structure.[32]

Other alleged LLCs reported in the literature are probably more aptly called "pseudo-LLCs." Those could be related to experimental artifacts (reviewed in ref.[205]) or transitions appearing above T_l that can be associated with dissolving solid-like remainders on heating.[206] In other cases,[15] probably crystallisation was mistaken for an LLC, including hysteresis.[16,17] For other transitions that have been called glass-to-glass transition, like the hydrogen-induced transition in Mg-Ce-Ni-based glasses,[207] it remains open into which category they are to be placed.

6.3. Vitrification

That upon annealing of metallic glasses, the temperature dependence of in-situ-obtained structural metrics, mainly those in reciprocal space, shows a kink close to T_g (known from thermo-analytical methods) has been shown and discussed in the literature galore.[34,35,48–52,55–58,164,198,208–210] Similar observations were made for oxide glasses.[211] The studies investigating the glass transition of metallic-glass-forming liquids on cooling from the high-temperature equilibrium liquid found comparable kinks at T_g. Detailed discussions of the evolving structural metrics across vitrification showed similar kinks in reciprocal as well as real space.[153] Again, similar results for oxide glasses on cooling were reported as well.[19,20,212]

Below T_g, for annealing as well as cooling experiments and simulations, structural metrics show mostly linear or even constant temperature dependence.[34,35,37,46,47,50–52] This can be interpreted to result from ordinary thermal expansion of the glass after the structural changes in the undercooled liquid have ceased to dominate. Especially the almost constant FWHM Γ_1 of the first halo points to mainly the Debye-Waller factor acting[46] and shows that the increase of the structural correlation length $\propto 2\pi/\Gamma_1$ during undercooling has stopped. Although it is beneficial to be principally able to identify the glass transition from structural results *via* the kink, a direct comparison of structural functions somewhat above as well as below T_g yields almost no differences, highlighting again Anderson's puzzle. Since to date no partial structures

have been experimentally resolved in pathway studies, for an insight on what causes the liquid to freeze into a glass at T_g simulation results are inevitable.

Several MD simulation studies clearly replicate the kink at or around T_g (Figure 15), where the rapid increase in numbers of clusters abruptly stops.[45,165,170,194,213] Nonstructural results like diffusion coefficients derived from MD simulations show abrupt changes close to T_g as well.[25,194] The developing backbones in the form of networks of clusters[186,188,189,194,197] mentioned above seem to be the responsible entity that slows down the kinetics and causes the large increase in the activation energy and viscosity.[193] Arrest occurs close to or at T_g and vitrificaction takes place. The addition of relatively small quantities of alloying elements, Al to Zr-Cu-based metallic glasses being a prominent example,[45,214] can enhance cluster formation as well as their interconnection, leading to increased GFA.[45,165–167,189] Indications for possible first-order glass transitions have been reported.[80,203]

Using T_l (or T_m) and T_g the pathway can be divided into the three regimes (Figure 16d). However, considering possible LLCs at T_{LLC}, another possible way of a division, again into three regimes, is possible (Figure 16b,c). Now the regime of the high-T liquid (HTL) on cooling does not necessarily end at T_l or T_m, but may extend down to T_{LLC}. The second regime is between T_{LLC} and T_g, which may be called low-T liquid (LTL),[18,200] which is followed by the glassy regime below T_g. A division in this way has been pointed out for metallic glasses in simulation and experiment as well as for oxide glasses.[18,19,25,45,50,51,194] The three regimes have also been likened[45] to the Angell et al.'s three "domains of interest" during cooling of glass-forming materials.[31,215] Future investigations have to validate this possible correspondence as well as if the existence of three regimes along the pathway is a general phenomenon. Together with further characteristic temperatures, like T_A in the high-temperature liquid[9] even more domains or regimes may be distinguished depending on the details of the topology of the potential energy landscape of the particular material.[25] Several results from MD simulations show accelerated structural ordering in the second regime, mainly ascribed to the formation of clusters of icosahedral-like geometry (Figure 12).[45,165,167,170] This is supposed to be especially the case the more fragile the melt is (Figure 16b). It is worthwhile mentioning that in an alternative view, the dominance of the icosahedral structural motif is to be considered a sign of nano-crystallisation rather than one of glass formation.[216]

7. Outlook

Although still a young field, in-situ monitoring of structural changes during undercooling of metallic melts, including liquid-liquid crossovers and vitrification itself, has already yielded intriguing and important results. The main advantage of the structural measurements, as opposed to, e.g., viscosity measurements, is the possibility to gain detailed insights for the complete pathway of a liquid alloy to vitrification within a single experiment. Combined with simulations, it could be shown that during undercooling, clusters and their interconnection evolve, being responsible for the viscous slowdown and LLCs. It is, however, still not clear what exactly determines the value of T_g, i.e., what condition has been met at this temperature that the structure locks into place. Anderson's puzzle has still not been fully solved. However, it has to be considered that in-situ vitrification, after following the complete pathway, has only been reported for ten alloys from a limited number of alloy systems so far (Table 1). More such measurements for much wider classes of glasses (metallic and non-metallic) and related simulations are necessary to identify or verify universalities in their structural behaviour. Even if not the complete pathway, but still a sufficiently wide temperature range, can be captured, valuable information towards universalities can be obtained. Already now, the acceleration of the structural evolution during undercooling was observed in several alloy systems for which only incomplete data is available (e.g., Ni-Nb[159,161] (cf. also Figure 11c), Ni-Nb-Ta,[159] Cu-Hf[64]) pointing to general trends. Further supporting studies, utilising new setups and methods, need to be carried out.

For X-ray investigations at synchrotrons and free-electron lasers, it is mainly the desire for element-specific measurements, to obtain partial structure factors. At first sight it seems that AXS could be a relatively simple way to achieve this goal. However, the same experiment, i.e., following the pathway in the exact same manner, would need to be meticulously repeated several times with different wavelengths for the different elements in the sample. Alternatively, a setup for the *simultaneous* acquisition with different wavelengths, similar to what was recently proposed and demonstrated for other X-ray techniques,[217–222] would need to be devised. Additionally, the relevant absorption edges of many elements are too low to cover a wide Q range (Eqs. (1) and (4)).[114] Nevertheless, any additional information, e.g., to inform RMC simulations, is of interest.

Investigating alloys with low GFA calls for much smaller sample sizes, causing much higher cooling rates.

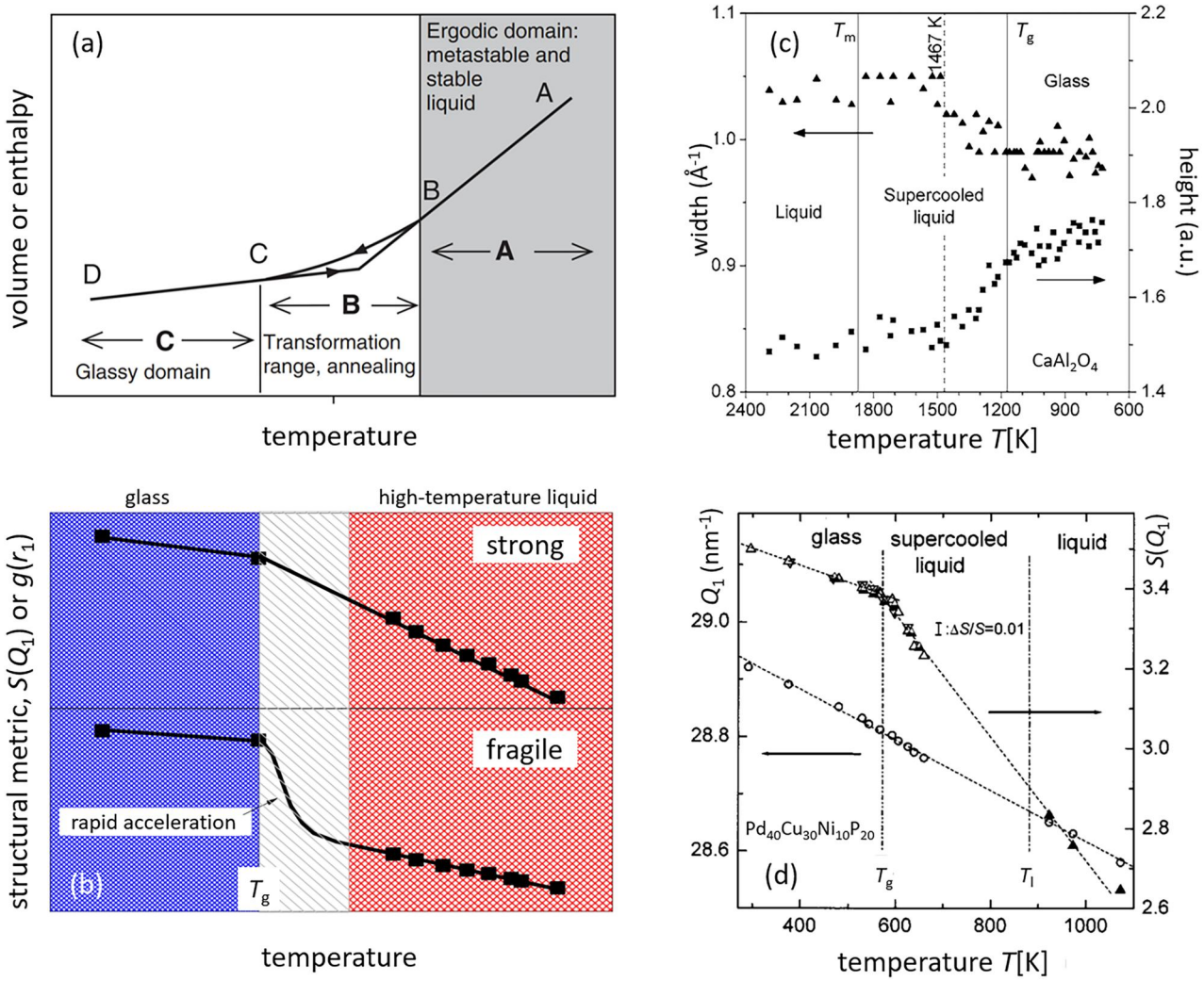


Figure 16. The pathway of liquids to vitrification can be separated into three different regimes. This subdivision is not unique and not agreed upon. Parallels to Angell's three domains of interest[31,215] can be drawn (a, adapted with permission from ref. [31]) Mauro et al. (cf., e.g., ref. [160]) hinted at three regimes, where the evolution of structural metrics in the region between high-temperature liquid and glass supposedly depends on the materials fragility (b, adapted with permission from ref. [160]) Three regimes have also been pointed out for oxide melts (c, here $CaAl_2O_4$ adapted with permission from ref. [19] mind the flipped temperature scale). A possible LLC in the undercooled ("supercooled") regime ($T_{LLC} = 1467$ K) and not T_m (or T_l) maybe the actual border of the first two regimes on cooling. Three regimes (glass, undercooled ("supercooled") liquid and liquid) have also been discussed for heating experiments (d, here $Pd_{40}Cu_{30}Ni_{10}P_{20}$, note how position Q_1 and height $S(Q_1)$ are affected very differently across the glass transition; adapted with permission from ref. [35]).

XFELs could be immensely beneficial in this respect, as necessary small exposure times are compensated by higher intensity to keep the SNR sufficiently high.[125,126] As the high intensity of the X-rays from XFELs destroys the sample after each diffraction pattern, a pump-probe-like experiment needs to be used. Therein, the sample would be heated up, e.g., by a laser pulse, to a desired temperature T_{start} where the pathway commences. Following the deactivation of the heating, a single diffraction pattern would be recorded after a certain delay time at a temperature below T_{start}. In this way, the complete pathway would not be probed in one continuous run but as a series of many diffraction patterns, each taken after a slightly longer delay time. A connected challenge lies in the automated and sufficiently fast continued supply of samples of well-defined mass. Pump-probe methods could also benefit AXS measurements needing different X-ray wavelengths, as discussed above. Together with faster detectors, having better SNR and energy discrimination, identification of structural signatures of vitrification and LLCs of a much wider spectrum of alloy compositions would be possible.

Complementing the wide-angle measurements reviewed here, SAXS along the complete pathway, maybe even simultaneously,[223] would provide further and more direct insight into the different length scales that

govern the structural changes during LLCs and vitrification.[163] A further boost to studying the pathway in particular and the structure of (not only) glasses in general may be provided by the future prospect of a possible day-to-day use of compact X-ray sources.[224–226]

Since neutron sources and detectors that allow for a time resolution to cover the complete pathway, as can be done with synchrotron radiation, are not to be expected anytime soon, let alone compact variants thereof, electrons as probes should be revisited. Recent advances have been made to use this method for the investigation of fast structural changes.[111,227,228] The use of electrons can be considered twofold. On the one hand, electron scattering provides additional information to disentangle the partial structure factors (here the size of the facility is of minor relevance, and accelerator-based setups would be acceptable[111,228,229]). On the other hand, as compact in-house total-scattering method, e.g., in modified transmission electron microscopes (TEM)[227] "replacing" synchrotrons. Since transmission electron diffraction in a TEM can only work properly with sample thicknesses up to $\approx$ 100 nm, levitating (and keeping the beam focussed onto) samples of this size is virtually excluded. Additionally, levitation is also excluded since the sample needs to be properly grounded and also because the default configuration of TEMs uses vertical electron beams. Other reasons that prevent the use of levitation setups for electron diffraction have been mentioned above. Interestingly, vitrification of nm-sized metallic samples *without* using containerless levitation has been achieved recently.[230,231] However, as discussed above in relation to XFELs, such small sample sizes lead to much higher cooling rates, making it virtually impossible to record the complete pathway in a single run. Again, a pump-probe-like experiment could be used. Appropriate samples could, for instance, be prepared using FIB (focussed ion beam) and heated by pulses of electrical current.[230] As even the vitrification of nm-sized pure metals (connected to a heat sink) could be demonstrated,[230] such a technique is promising to work for most metallic-glass-forming alloys. Contrary to the procedure using XFELs as described above, the sample could even be re-heated to T_{start} whereafter the next measurement is taken after a slightly longer delay time. However, a possible deterioration of the sample during cycling in the pump-probe experiments, mainly by evaporation, may need to be taken into account. Progress in the development of direct electron-detectors[232–236] with high SNR could massively aid this method. However, electron diffraction alone would not allow for partial structure factors to be resolved. This issue could, again, be mitigated by using a pump-probe setup for EXELFS (extended electron energy loss fine structure[235,237–239]) as an energy-dispersive technique, analogous to EXAFS. These developments may turn electrons into a valuable tool to monitor the pathway and in-situ vitrification after all.

As briefly mentioned in Section 3, the studies discussed do not take into account inelastic scattering separately and, hence, a possible influence of the dynamic structure on the vitrification. With the abovementioned "structural Curie-Weiss behaviour," the promising attempt for a comprehensive framework to describe the combined structural and dynamical influences at different length scales on glass formation and vitrification has been introduced recently.[37,154,180,193,216,240–245] Although experimental techniques like inelastic X-ray/neutron scattering or X-ray photon correlation spectroscopy (XPCS) can access dynamic contributions, the required speed along the pathway, again, imposes limitations. However, isothermal holds or pump-probe setups can help to address this issue.

Also, as mentioned briefly earlier, structural milestones along the pathway should be backed up by measurements of complementary properties. Ideally, those measurements would need to be carried out in the same setup or even parallel to the diffraction experiments. In any case, those multi-messenger studies should be performed more frequently. While some of those combined measurements have been reported as already mentioned (density,[246,247] thermal expansion, specific heat,[23,102] electrical resistivity,[22,23] viscosity,[76,82,247] surface tension[76,82–84]) further combinations are thinkable, even if not the complete pathway can be captured. Such a possible method could be nuclear magnetic resonance (NMR) spectroscopy. For oxide glasses, NMR is used in CNL setups already.[248,249] In metals it is foremost the so-called Knight shift that is measured by NMR.[250] Although not in levitation experiments, for $La_{50}Al_{35}Ni_{15}$ it was shown that the Knight shift can highlight signatures of a crossover above T_l[251] and for $Pd_{43}Ni_{10}Cu_{27}P_{20}$ above T_g.[252] Also, MD and RMC simulations carried out for as many temperatures along the pathway as possible and with small increments can give valuable insights. Here the ever-increasing power of modern computers will be an asset.

In-situ studies with varying cooling rates need to be performed more often. On the one hand, since the cooling-rate dependence of LLCs needs to be investigated further. In this respect, alloys that have been vitrified using ESL should also be investigated in a CNL setup. On the other hand, a low enough cooling rate will lead to crystallisation and the analysis of the emerging crystal structures may, e.g., help to learn

more about the SRO in the related liquid and glass as well. Furthermore, a comparison with crystalline structures that emerge during annealing an already prepared glass is supposed to yield insights on the prerequisites for high GFA if its relation to a competition of crystalline structures is kept in mind.[253] Although preliminary results exist[60] a detailed analysis is still missing.

Additionally, independent of the particular type of experiment, the investigated temperature range should be extended on both ends of the pathway. For high temperatures, this is necessary to examine how far the found non-linear behaviour of structural metrics continues and how common anomalies that point to LLCs above T_l[254,255] are. Going to temperatures way below T_g *in situ* after vitrification would be intriguing as well. To monitor possible further structural changes[256,257] down to cryogenic temperatures, reducing the temperature of the gas stream in a CNL setup could be supplemented by a cooled sample holder that "grabs" the already vitrified sample *in situ*, providing additional conductive cooling.

Finally, going the pathway in the opposite direction will be insightful as well, i.e., heating the glass rapidly enough to bypass crystallisation ending up at temperatures above T_l. This "up-quenching"[258] has been demonstrated using ultrafast chip calorimetry, but results in combination with ultrafast structural investigations showing the absence of crystallinity are yet to be published.[259]

Disclosure statement

No potential conflict of interest was reported by the author(s).

Funding

We wish to acknowledge financial support in part from the EPSRC-DTP studentship "Bulk Metallic Glasses: Revealing the Structural Pathway of Liquid Metals to Vitrification" [project reference 2043971] within the framework of the EPSRC Doctoral Training Partnership with Cranfield University [EP/N509450/1] and in part from the Cranfield University 75th Anniversary Research Fellowship scheme.

ORCID

Martin E. Stiehler http://orcid.org/0000-0002-6941-2025
Konstantinos Georgarakis http://orcid.org/0000-0003-0918-7310

References

1. Anderson, P. W. Through the Glass Lightly. *Science* **1995**, *267*, 1615–1616. doi:10.1126/science.267.5204.1615-e.
2. Greer, A. L. Metallic Glasses … on the Threshold. *Mater. Today* **2009**, *12*, 14–22. doi:10.1016/S1369-7021(09)70037-9.
3. Hofmann, D. C.; Polit-Casillas, R.; Roberts, S. N.; Borgonia, J. P.; Dillon, R. P.; Hilgemann, E.; Kolodziejska, J.; Montemayor, L.; Suh, J. O.; Hoff, A.; et al. Castable Bulk Metallic Glass Strain Wave Gears: Towards Decreasing the Cost of High-Performance Robotics. *Sci. Rep.* **2016**, *6*, 37773. doi:10.1038/srep37773.
4. Khan, M. M.; Nemati, A.; Rahman, Z. U.; Shah, U. H.; Asgar, H.; Haider, W. Recent Advancements in Bulk Metallic Glasses and Their Applications: A Review. *Crit. Rev. Solid State* **2018**, *43*, 233–268. doi:10.1080/10408436.2017.1358149.
5. Gao, K.; Zhu, X.; Chen, L.; Li, W.; Xu, X.; Pan, B.; Li, W.; Zhou, W.; Li, L.; Huang, W.; Li, Y. Recent Development in the Application of Bulk Metallic Glasses. *J. Mater. Sci. Technol.* **2022**, *131*, 115–121. doi:10.1016/j.jmst.2022.05.028.
6. Sohrabi, S.; Fu, J.; Li, L.; Zhang, Y.; Li, X.; Sun, F.; Ma, J.; Wang, W. H.; Wang, W. H. Manufacturing of Metallic Glass Components: Processes, Structures and Properties. *Prog. Mater. Sci.* **2024**, *144*, 101283. doi:10.1016/j.pmatsci.2024.101283.
7. Stiehler, M. E.; Georgarakis, K. Metallic Glasses–Novel Materials for Applications in Nuclear Fusion. *IEEE Trans. Plasma Sci.* **2024**, *52*, 4161–4166. doi:10.1109/TPS.2024.3459809.
8. Wendt, H. R.; Abraham, F. F. Empirical Criterion for the Glass Transition Region Based on Monte Carlo Simulations. *Phys. Rev. Lett.* **1978**, *41*, 1244–1246. doi:10.1103/PhysRevLett.41.1244.
9. Jaiswal, A.; Egami, T.; Kelton, K. F.; Schweizer, K. S.; Zhang, Y. Correlation between Fragility and the Arrhenius Crossover Phenomenon in Metallic, Molecular, and Network Liquids. *Phys. Rev. Lett.* **2016**, *117*, 205701. doi:10.1103/PhysRevLett.117.205701.
10. Hennet, L.; Cristiglio, V.; Kozaily, J.; Pozdnyakova, I.; Fischer, H. E.; Bytchkov, A.; Drewitt, J. W.; Leydier, M.; Thiaudière, D.; Gruner, S.; et al. Aerodynamic Levitation and Laser Heating: Applications at Synchrotron and Neutron Sources. *Eur. Phys. J. Spec. Top.* **2011**, *196*, 151–165. doi:10.1140/epjst/e2011-01425-0.
11. Benmore, C. J. A Review of High-Energy X-Ray Diffraction from Glasses and Liquids. *ISRN Mater. Sci.* **2012**, *2012*, 1–19. doi:10.5402/2012/852905.
12. Benmore, C. J.; Weber, J. K. Aerodynamic Levitation, Supercooled Liquids and Glass Formation. *Adv. Phys. X* **2017**, *2*, 717. doi:10.1080/23746149.2017.1357498.
13. Hennet, L.; Holland Moritz, D.; Weber, R.; Meyer, A. High-Temperature Levitated Materials. In *Experimental Methods in the Physical Sciences*, 1st ed.; Elsevier Inc.: Amsterdam, **2017**; Vol. 49, pp. 583–636. doi:10.1016/B978-0-12-805324-9.00010-8.
14. Huang, S.; Xiang, K.; Mi, J. Recent Advances in Synchrotron X-Ray Studies of the Atomic Structures of Metal Alloys in Liquid State. *J. Mater. Sci.*

Technol. **2024**, *203*, 180–200. doi:10.1016/j.jmst.2024.02.038.
15. Li, J. J. Z.; Rhim, W. K.; Kim, C. P.; Samwer, K.; Johnson, W. L. Evidence for a Liquid-Liquid Phase Transition in Metallic Fluids Observed by Electrostatic Levitation. *Acta Mater.* **2011**, *59*, 2166–2171. doi:10.1016/j.actamat.2010.12.017.
16. Bendert, J. C.; Blodgett, M. E.; Gangopadhyay, A. K.; Kelton, K. F. Measurements of Volume, Thermal Expansion, and Specific Heat in $Zr_{57}Cu_{15.4}Ni_{12.6}Al_{10}Nb_5$ and $Zr_{58.5}Cu_{15.6}Ni_{12.8}Al_{10.3}Nb_{2.8}$ Liquids and Glasses. *Appl. Phys. Lett.* **2013**, *102*, 211913. doi:10.1063/1.4808030.
17. Wei, S.; Yang, F.; Bednarcik, J.; Kaban, I.; Shuleshova, O.; Meyer, A.; Busch, R. Liquid-Liquid Transition in a Strong Bulk Metallic Glass-Forming Liquid. *Nat. Commun.* **2013**, *4*, 2083. doi:10.1038/ncomms3083.
18. Stolpe, M.; Jonas, I.; Wei, S.; Evenson, Z.; Hembree, W.; Yang, F.; Meyer, A.; Busch, R. Structural Changes during a Liquid-Liquid Transition in the Deeply Undercooled $Zr_{58.5}Cu_{15.6}Ni_{12.8}Al_{10.3}Nb_{2.8}$ Bulk Metallic Glass Forming Melt. *Phys. Rev. B.* **2016**, *93*, 014201. doi:10.1103/PhysRevB.93.014201.
19. Hennet, L.; Pozdnyakova, I.; Bytchkov, A.; Price, D. L.; Greaves, G. N.; Wilding, M.; Fearn, S.; Martin, C. M.; Thiaudière, D.; Bérar, J.-F.; et al. Development of Structural Order During Supercooling of a Fragile Oxide Melt. *J. Chem. Phys.* **2007**, *126*, 074906. doi:10.1063/1.2646812.
20. Bytchkov, A.; Hennet, L.; Pozdnyakova, I.; Wright, J.; Vaughan, G.; Rossano, S.; Madjer, K.; Price, D. L. Filming Vitrification with ms Time Resolution. *AIP Conf. Proc.* **2010**, *1234*, 219. doi:10.1063/1.3463177.
21. Benmore, C. J.; González, G. B.; Alderman, O. L. G.; Wilke, S. K.; Yarger, J. L.; Leinenweber, K.; Weber, J. K. R. Hard x-Ray Methods for Studying the Structure of Amorphous Thin Films and Bulk Glassy Oxides. *J. Phys. Condens. Matter.* **2021**, *33*, 194001. doi:10.1088/1361-648x/abe352.
22. Van Hoesen, D. C.; Gangopadhyay, A. K.; Lohöfer, G.; Sellers, M. E.; Pueblo, C. E.; Koch, S.; Galenko, P. K.; Kelton, K. F. Resistivity Saturation in Metallic Liquids Above a Dynamical Crossover Temperature Observed in Measurements Aboard the International Space Station. *Phys. Rev. Lett.* **2019**, *123*, 226601. doi:10.1103/PhysRevLett.123.226601.
23. Mohr, M.; Wunderlich, R. K.; Hofmann, D. C.; Fecht, H. J. Thermophysical Properties of Liquid $Zr_{52.5}Cu_{17.9}Ni_{14.6}Al_{10}Ti_5$ - Prospects for Bulk Metallic Glass Manufacturing in Space. *NPJ Microgravity* **2019**, *5*, 24. doi:10.1038/s41526-019-0084-1.
24. Zhang, C.; Hu, L.; Yue, Y.; Mauro, J. C. Fragile-to-Strong Transition in Metallic Glass-Forming Liquids. *J. Chem. Phys.* **2010**, *133*, 014508. doi:10.1063/1.3457670.
25. Alvarez-Donado, R.; Cajahuaringa, S.; Antonelli, A. Revisiting the Fragile-to-Strong Crossover in Metallic Glass-Forming Liquids: Application to $Cu_xZr_xAl_{100-2x}$ Alloy. *Phys. Rev. Mater.* **2019**, *3*, 085601. doi:10.1103/PhysRevMaterials.3.085601.
26. Lucas, P. Fragile-to-Strong Transitions in Glass Forming Liquids. *J. Non-Cryst. Solids X* **2019**, *4*, 100034. doi:10.1016/j.nocx.2019.100034.
27. Wei, S.; Yang, F.; Bednarcik, J.; Kaban, I.; Meyer, A.; Busch, R. Polyamorphous Transformation in Bulk Metallic Glass-Forming Liquid and Its Implication to Strong Liquids. *AIP Conf. Proc.* **2013**, *1518*, 260. doi:10.1063/1.4794577.
28. Wang, X.-D.; Jiang, J.-Z. Perspective on Structural Evolution and Relations with Thermophysical Properties of Metallic Liquids. *Adv. Mater.* **2017**, *29*, 1703136. doi:10.1002/adma.201703136.
29. Lucas, P.; Wei, S.; Angell, C. A. Liquid-Liquid Phase Transitions in Glass-Forming Systems and Their Implications for Memory Technology. *Int. J. Appl. Glass Sci.* **2020**, *11*, 236–244. doi:10.1111/ijag.15109.
30. Tanaka, H. General View of a Liquid-Liquid Phase Transition. *Phys. Rev. E Stat. Phys. Plasmas. Fluids. Relat. Interdiscip. Topics.* **2000**, *62*, 6968–6976. doi:10.1103/PhysRevE.62.6968.
31. Angell, C. Glass-Formers and Viscous Liquid Slowdown Since David Turnbull: Enduring Puzzles and New Twists. *MRS Bull.* **2008**, *33*, 544–555. doi:10.1557/mrs2008.108.
32. Tanaka, H. Liquid-Liquid Transition and Polyamorphism. *J. Chem. Phys.* **2020**, *153*, 130901. doi:10.1063/5.0021045.
33. Uriarte, J.; Yavari, A.; Nishiyama, N.; Heunen, G.; Vaughan, G.; Kvick, Å.; Inoue, A. In-the-Beam Metallic Glass Formation Monitored by High-Energy Synchrotron Radiation. *Scr. Mater.* **2003**, *48*, 809–812. doi:10.1016/S1359-6462(02)00533-X.
34. Yavari, A. R.; Nikolov, N.; Nishiyama, N.; Zhang, T.; Inoue, A.; Uriarte, J. L.; Heunen, G. The Glass Transition of Bulk Metallic Glasses Studied by Real-Time Diffraction in Transmission Using High-Energy Synchrotron Radiation. *Mater. Sci. Eng. A* **2004**, *375-377*, 709–712. doi:10.1016/j.msea.2003.10.224.
35. Mattern, N.; Hermann, H.; Roth, S.; Sakowski, J.; Macht, M.-P.; Jovari, P.; Jiang, J. Structural Behavior of $Pd_{40}Cu_{30}Ni_{10}P_{20}$ Bulk Metallic Glass Below and Above the Glass Transition. *Appl. Phys. Lett* **2003**, *82*, 2589–2591. doi:10.1063/1.1567457.
36. Nishiyama, N.; Takenaka, K.; Miura, H.; Saidoh, N.; Zeng, Y.; Inoue, A. The World's Biggest Glassy Alloy Ever Made. *Intermetallics* **2012**, *30*, 19–24. doi:10.1016/j.intermet.2012.03.020.
37. Ryu, C. W.; Dmowski, W.; Kelton, K. F.; Lee, G. W.; Park, E. S.; Morris, J. R.; Egami, T. Curie-Weiss Behavior of Liquid Structure and Ideal Glass State. *Sci. Rep.* **2019**, *9*, 18579. doi:10.1038/s41598-019-54758-y.
38. Pajor, K.; Kozieł, T.; Cios, G.; Błyskun, P.; Bała, P.; Zielińska-Lipiec, A. Glass Forming Ability of the $Zr_{50}Cu_{40}Al_{10}$ Alloy with Two Oxygen Levels. *J. Non-Cryst. Solids* **2018**, *496*, 42–47. doi:10.1016/j.jnoncrysol.2018.05.034.
39. Watanabe, M.; Mizuno, A.; Akimoto, T.; Kohara, S. In-Situ Observation of Solidification of Bulk Metallic Glass Forming Alloys from Supercooled Liquid by Using High Energy X-Ray Diffraction Combined

with Levitation Techniques. *MSF.* **2010**, *638-642*, 1677–1682. doi:10.4028/www.scientific.net/MSF.638-642.1677.

40. Qu, D.; Mizuno, A.; Watanabe, M.; Bednarcik, J.; Shen, J. Undercooling Behavior of Zr-Cu-Ni-Al Bulk Metallic Glasses Investigated by in Situ Synchrotron High Energy X-Ray Diffraction. *Mater. Sci. Eng. A* **2012**, *555*, 36–43. doi:10.1016/j.msea.2012.06.030.
41. Haruyama, O.; Nakayama, Y.; Wada, R.; Tokunaga, H.; Okada, J.; Ishikawa, T.; Yokoyama, Y. Volume and Enthalpy Relaxation in $Zr_{55}Cu_{30}Ni_5Al_{10}$ Bulk Metallic Glass. *Acta Mater.* **2010**, *58*, 1829–1836. doi:10.1016/j.actamat.2009.11.025.
42. Louzguine-Luzgin, D.; Georgarakis, K.; Andrieux, J.; Hennet, L.; Morishita, T.; Nishio, K.; Belosludov, R. An Atomistic Study of the Structural Changes in a Zr-Cu-Ni-Al Glass-Forming Liquid on Vitrification Monitored *In-Situ* by X-Ray Diffraction and Molecular Dynamics Simulation. *Intermetallics* **2020**, *122*, 106795. doi:10.1016/j.intermet.2020.106795.
43. Lan, S.; Blodgett, M.; Kelton, K. F.; Ma, J. L.; Fan, J.; Wang, X. L. Structural Crossover in a Supercooled Metallic Liquid and the Link to a Liquid-to-Liquid Phase Transition. *Appl. Phys. Lett* **2016**, *108*, 211907. doi:10.1063/1.4952724.
44. Wei, S.; Stolpe, M.; Gross, O.; Evenson, Z.; Gallino, I.; Hembree, W.; Bednarcik, J.; Kruzic, J. J.; Busch, R. Linking Structure to Fragility in Bulk Metallic Glass-Forming Liquids. *Appl. Phys. Lett.* **2015**, *106*, 181901. doi:10.1063/1.4919590.
45. Georgarakis, K.; Hennet, L.; Evangelakis, G.; Antonowicz, J.; Bokas, G.; Honkimaki, V.; Bytchkov, A.; Chen, M.; Yavari, A. Probing the Structure of a Liquid Metal During Vitrification. *Acta Mater.* **2015**, *87*, 174–186. doi:10.1016/j.actamat.2015.01.005.
46. Georgarakis, K.; Stiehler, M. E.; Hennet, L.; Guo, Y.; Antonowicz, J.; Louzguine-Luzgin, D. V.; Jolly, M. R.; Andrieux, J.; Vaughan, G. B.; Greer, A. L. *In-Situ* Monitoring the Structural Pathway of a Ti-Based Alloy from Metallic Liquid to Metallic Glass. *J. Alloy. Compd.* **2025**, *1025*, 180214. doi:10.1016/j.jallcom.2025.180214.
47. Mattern, N.; Kuhn, U.; Sakowski, J.; Neuefeind, J.; Eckert, J. Structure of $Zr_{52}Ti_5Cu_{18}Ni_{15}Al_{10}$ Bulk Metallic Glass at Elevated Temperatures. *Mater. Trans.* **2002**, *43*, 1947–1951. doi:10.2320/matertrans.43.1947.
48. Mattern, N.; Sakowski, J.; Kühn, U.; Vinzelberg, H.; Eckert, J. Structural Behavior and Glass Transition of Bulk Metallic Glasses. *J. Non-Cryst. Solids* **2004**, *345-346*, 758–761. doi:10.1016/j.jnoncrysol.2004.08.197.
49. Yavari, A. R.; Moulec, A. L.; Inoue, A.; Nishiyama, N.; Lupu, N.; Matsubara, E.; Botta, W. J.; Vaughan, G.; Michiel, M. D.; Kvick, Å. Excess Free Volume in Metallic Glasses Measured by X-Ray Diffraction. *Acta Mater.* **2005**, *53*, 1611–1619. doi:10.1016/j.actamat.2004.12.011.
50. Mattern, N.; Kühn, U.; Eckert, J. Structural Behavior of Amorphous and Liquid Metallic Alloys at Elevated Temperatures. *J. Non-Cryst. Solids* **2007**, *353*, 3327–3331. doi:10.1016/j.jnoncrysol.2007.05.079.
51. Jiang, Q.; Chang, Z.; Wang, X.; Jiang, J. Structures at Glassy, Supercooled Liquid, and Liquid States in La-Based Bulk Betallic Glasses. *Metall. Mater. Trans. A* **2010**, *41*, 1634–1639. doi:10.1007/s11661-009-0041-9.
52. Mattern, N.; Stoica, M.; Vaughan, G.; Eckert, J. Thermal Behaviour of $Pd_{40}Cu_{30}Ni_{10}P_{20}$ Bulk Metallic Glass. *Acta Mater.* **2012**, *60*, 517–524. doi:10.1016/j.actamat.2011.10.032.
53. Johnson, M.; Mauro, N.; Vogt, A.; Blodgett, M.; Pueblo, C.; Kelton, K. Structural Evolution and Thermophysical Properties of Zr_xNi_{100-x} Metallic Liquids and Glasses. *J. Non-Cryst. Solids* **2014**, *405*, 211–218. doi:10.1016/j.jnoncrysol.2014.10.026.
54. Yavari, A. R.; Moulec, A. L.; Nishiyama, N.; Inoue, A.; Vaughan, G.; Kvick, A.; Botta, W. J. Glass Transition Tg, and Quenched-in Free Volume in Bulk Metallic Glasses Measured by X-Ray Diffraction. *JMNM.* **2004**, *20-21*, 23–28. doi:10.4028/www.scientific.net/JMNM.20-21.23.
55. Bednarcik, J.; Michalik, S.; Sikorski, M.; Curfs, C.; Wang, X. D.; Jiang, J. Z.; Franz, H. Thermal Expansion of a La-Based Bulk Metallic Glass: Insight from *In-situ* High-Energy x-Ray Diffraction. *J. Phys: Condens. Matter* **2011**, *23*, 254204. doi:10.1088/0953-8984/23/25/254204.
56. Evenson, Z.; Naleway, S. E.; Wei, S.; Gross, O.; Kruzic, J. J.; Gallino, I.; Possart, W.; Stommel, M.; Busch, R. β relaxation and Low-Temperature Aging in a Au-Based Bulk Metallic Glass: From Elastic Properties to Atomic-Scale Structure. *Phys. Rev. B* **2014**, *89*, 174204. doi:10.1103/PhysRevB.89.174204.
57. Hechler, S.; Ruta, B.; Stolpe, M.; Pineda, E.; Evenson, Z.; Gross, O.; Bernasconi, A.; Busch, R.; Gallino, I. Microscopic Evidence of the Connection between Liquid-Liquid Transition and Dynamical Crossover in an Ultraviscous Metallic Glass Former. *Phys. Rev. Mater.* **2018**, *2*, 085603. doi:10.1103/PhysRevMaterials.2.085603.
58. Küchemann, S.; Derlet, P. M.; Liu, C.; Rosenthal, D.; Sparks, G.; Larson, W. S.; Maaß, R. Energy Storage in Metallic Glasses Via Flash Annealing. *Adv. Funct. Mater.* **2018**, *28*, 1805385. doi:10.1002/adfm.201805385.
59. Yavari, A. R.; Le Moulec, A.; Botta F, W. J.; Inoue, A.; Rejmankova, P.; Kvick, A. *In Situ* Crystallization of $Zr_{55}Cu_{30}Al_{10}Ni_5$ Bulk Glass Forming from the Glassy and Undercooled Liquid States Using Synchrotron Radiation. *J. Non-Cryst. Solids* **1999**, *247*, 31–34. doi:10.1016/S0022-3093(99)00027-7.
60. Georgarakis, K.; Yavari, A. R.; Louzguine-Luzgin, D. V.; Vaughan, G. Crystallization and Vitrification of a PdCuNiP Metallic Glass Upon Thermal and Mechanical Processes Detected by Synchrotron Light X-Ray Radiation. *AIP Conf. Proc.* **2013**, *1518*, 672. doi:10.1063/1.4794657.
61. Kosiba, K.; Rothkirch, A.; Han, J.; Deng, L.; Escher, B.; Wang, G.; Kühn, U.; Bednarcik, J. Phase Formation of a Biocompatible Ti-Based Alloy Under Kinetic Constraints Studied via in-Situ High-Energy X-Ray Diffraction. *Prog. Nat. Sci. Mater. Int.* **2020**, *30*, 432–436. doi:10.1016/j.pnsc.2020.06.004.
62. Krishnan, S.; Felten, J. J.; Rix, J. E.; Weber, J. K.; Nordine, P. C.; Beno, M. A.; Ansell, S.; Price, D. L.

Levitation Apparatus for Structural Studies of High Temperature Liquids Using Synchrotron Radiation. *Rev. Sci. Instrum.* **1997**, *68*, 3512–3518. doi:10.1063/1.1148315.

63. Gangopadhyay, A. K.; Lee, G. W.; Kelton, K. F.; Rogers, J. R.; Goldman, A. I.; Robinson, D. S.; Rathz, T. J.; Hyers, R. W. Beamline Electrostatic Levitator for *In Situ* High Energy x-Ray Diffraction Studies of Levitated Solids and Liquids. *Rev. Sci. Instrum.* **2005**, *76*, doi:10.1063/1.1932447.
64. Mauro, N. A.; Vogt, A. J.; Johnson, M. L.; Bendert, J. C.; Soklaski, R.; Yang, L.; Kelton, K. F. Anomalous Structural Evolution and Liquid Fragility Signatures in Cu-Zr and Cu-Hf Liquids and Glasses. *Acta Mater.* **2013**, *61*, 7411–7421. doi:10.1016/j.actamat.2013.08.047.
65. Millot, F.; Paradis, P. F.; Rifflet, J. C.; Ishikawa, T. Macroscopic Properties of Liquids at Very High Temperature. *IJMPT.* **2006**, *26*, 274. doi:10.1504/ijmpt.2006.009470.
66. Herlach, D. M.; Cochrane, R. F.; Egry, I.; Fecht, H. J.; Greer, A. L. Containerless Processing in the Study of Metallic Melts and Their Solidification. *Int. Mater. Rev.* **1993**, *38*, 273–347. doi:10.1179/095066093790326267.
67. Hyers, R. W.; Rogers, J. R. A Review of Electrostatic Levitation for Materials Research. *High Temp. Mater. Process.* **2008**, *27*, 461. doi:10.1515/HTMP.2008.27.6.461.
68. Price, D. L. *High-Temperature Levitated Materials*; Cambridge University Press, Cambridge, **2010**. doi:10.1017/CBO9780511730306.
69. Egry, I.; Holland-Moritz, D. Levitation Methods for Structural and Dynamical Studies of Liquids at High Temperatures. *Eur. Phys. J. Spec. Top.* **2011**, *196*, 131–150. doi:10.1140/epjst/e2011-01424-1.
70. Paradis, P. F.; Ishikawa, T.; Lee, G. W.; Holland-Moritz, D.; Brillo, J.; Rhim, W. K.; Okada, J. T. Materials Properties Measurements and Particle Beam Interactions Studies Using Electrostatic Levitation. *Mater. Sci. Eng. R Rep.* **2014**, *76*, 1–53. doi:10.1016/j.mser.2013.12.001.
71. Okress, E. C.; Wroughton, D. M.; Comenetz, G.; Brace, P. H.; Kelly, J. C. Electromagnetic Levitation of Solid and Molten Metals. *J. Appl. Phys.* **1952**, *23*, 545–552. doi:10.1063/1.1702249.
72. Mathiak, G.; Egry, I.; Hennet, L.; Thiaudière, D.; Pozdnyakova, I.; Price, D. Aerodynamic Levitation and Inductive Heating - A New Concept for Structural Investigations of Undercooled Melts. *Int. J. Thermophys.* **2005**, *26*, 1151–1166. doi:10.1007/s10765-005-6708-6.
73. Rhim, W.; Chung, S. K.; Barber, D.; Man, K. F.; Gutt, G.; Rulison, A.; Spjut, R. E. An Electrostatic Levitator for High-Temperature Containerless Materials Processing in 1-g. *Rev. Sci. Instrum.* **1993**, *64*, 2961–2970. doi:10.1063/1.1144475.
74. Millikan, R. A. The Isolation of an Ion, a Precision Measurement of Its Charge, and the Correction of Stokes's Law. *Phys. Rev. (Series I)* **1911**, *32*, 349–397. doi:10.1103/PhysRevSeriesI.32.349.
75. Kelton, K. F.; Lee, G. W.; Gangopadhyay, A. K.; Hyers, R. W.; Rathz, T. J.; Rogers, J. R.; Robinson, M. B.; Robinson, D. S. First X-Ray Scattering Studies on Electrostatically Levitated Metallic Liquids: Demonstrated Influence of Local Icosahedral Order on the Nucleation Barrier. *Phys. Rev. Lett.* **2003**, *90*, 195504. doi:10.1103/PhysRevLett.90.195504.
76. Paradis, P. F.; Ishikawa, T.; Yoda, S. Surface Tension and Viscosity of Liquid and Undercooled Tantalum Measured by a Containerless Method. *J. Appl. Phys.* **2005**, *97*, 1. doi:10.1063/1.1854211.
77. Clancy, P.; Lierke, E.; Grossbach, R.; Heide, W. Electrostatic and Acoustic Instrumentation for Material Science Processing in Space. *Acta Astronaut.* **1980**, *7*, 877–891. doi:10.1016/0094-5765(80)90077-6.
78. Aoki, H.; Paradis, P. F.; Ishikawa, T.; Aoyama, T.; Masaki, T.; Yoda, S.; Ishii, Y.; Itami, T. Development of an Electrostatic Levitator for Neutron Diffraction Structure Analysis. *Rev. Sci. Instrum.* **2003**, *74*, 1147–1149. doi:10.1063/1.1531824.
79. Ishikawa, T.; Paradis, P.-F.; Yoda, S. New Sample Levitation Initiation and Imaging Techniques for the Processing of Refractory Metals with an Electrostatic Levitator Furnace. *Rev. Sci. Instrum.* **2001**, *72*, 2490–2495. doi:10.1063/1.1368861.
80. Busch, R.; Kim, Y. J.; Johnson, W. L.; Rulison, A. J.; Rhim, W. K.; Isheim, D. Hemispherical Total Emissivity and Specific Heat Capacity of Deeply Undercooled $Zr_{41.2}Ti_{13.8}Cu_{12.5}Ni_{10.0}Be_{22.5}$ Melts. *Appl. Phys. Lett.* **1995**, *66*, 3111. doi:10.1063/1.113619.
81. Gangopadhyay, A. K.; Kelton, K. F. Measurements of the Temperature-Dependent Total Hemispherical Emissivity Using an Electrostatic Levitation Facility. *Int. J. Thermophys.* **2017**, *38*, 3. doi:10.1007/s10765-016-2138-x.
82. Rhim, W. K.; Ohsaka, K.; Paradis, P. F.; Spjut, R. E. Noncontact Technique for Measuring Surface Tension and Viscosity of Molten Materials Using High Temperature Electrostatic Levitation. *Rev. Sci. Instrum.* **1999**, *70*, 2796–2801. doi:10.1063/1.1149797.
83. Rhim, W. K.; Ishikawa, T. Noncontact Surface Tension Measurement by Drop Rotation. *Rev. Sci. Instrum.* **2001**, *72*, 3572–3575. doi:10.1063/1.1388215.
84. Millot, F.; Rifflet, J. C.; Wille, G.; Sarou-Kanian, V.; Glorieux, B. Analysis of Surface Tension from Aerodynamic Levitation of Liquids. *J. Am. Ceram. Soc.* **2002**, *85*, 187–192. doi:10.1111/j.1151-2916.2002.tb00064.x.
85. Greaves, G. N.; Wilding, M. C.; Fearn, S.; Langstaff, D.; Kargl, F.; Cox, S.; Van, Q. V.; Majerus, O.; Benmore, C. J.; Weber, R.; et al. Detection of First-Order Liquid/Liquid Phase Transitions in Yttrium Oxide-Aluminum Oxide Melts. *Science* **2008**, *322*, 566–570. doi:10.1126/science.1160766.
86. Hennet, L.; Pozdnyakova, I.; Bytchkov, A.; Cristiglio, V.; Palleau, P.; Fischer, H. E.; Cuello, G. J.; Johnson, M.; Melin, P.; Zanghi, D.; et al. Levitation Apparatus for Neutron Diffraction Investigations on High

Temperature Liquids. *Rev. Sci. Instrum.* **2006**, *77*, doi:10.1063/1.2200756.
87. Ishikawa, T.; Paradis, P. F. Challenges of Handling, Processing, and Studying Liquid and Supercooled Materials at Temperatures Above 3000 K with Electrostatic Levitation. *Crystals* **2017**, *7*, 309. doi:10.3390/cryst7100309.
88. Neuville, D. R.; Hennet, L.; Florian, P.; de Ligny, D. *In Situ* High-Temperature Experiments. *Rev. Mineral. Geochem.* **2014**, *78*, 779–800. doi:10.2138/rmg.2013.78.19.
89. Cuello, G. J.; Cristiglio, V.; Hennet, L.; Puente-Orench, I. Neutron Scattering at High Temperature and Levitation Techniques. *J. Phys: Conf. Ser.* **2014**, *549*, 012002. doi:10.1088/1742-6596/549/1/012002.
90. Weber, J. K.; Tamalonis, A.; Benmore, C. J.; Alderman, O. L.; Sendelbach, S.; Hebden, A.; Williamson, M. A. Aerodynamic Levitator for *In Situ* x-Ray Structure Measurements on High Temperature and Molten Nuclear Fuel Materials. *Rev. Sci. Instrum.* **2016**, *87*, 073902. doi:10.1063/1.4955210.
91. Weber, H.; Schumacher, M.; Jóvári, P.; Tsuchiya, Y.; Skrotzki, W.; Mazzarello, R.; Kaban, I. Experimental and ab Initio Molecular Dynamics Study of the Structure and Physical Properties of Liquid GeTe. *Phys. Rev. B.* **2017**, *96*, 054204. doi:10.1103/PhysRevB.96.054204.
92. Winborne, D. A.; Nordine, P. C.; Rosner, D. E.; Marley, N. F. Aerodynamic Levitation Technique for Containerless High Temperature Studies on Liquid and Solid Samples. *Metall. Trans. B.* **1976**, *7*, 711–713. doi:10.1007/BF02698607.
93. Weber, J. K.; Hampton, D. S.; Merkley, D. R.; Rey, C. A.; Zatarski, M. M.; Nordine, P. C. Aero-Acoustic Levitation: A Method for Containerless Liquid-Phase Processing at High Temperatures. *Rev. Sci. Instrum.* **1994**, *65*, 456–465. doi:10.1063/1.1145157.
94. Nordine, P. C.; Merkley, D.; Sickel, J.; Finkelman, S.; Telle, R.; Kaiser, A.; Prieler, R. A Levitation Instrument for Containerless Study of Molten Materials. *Rev. Sci. Instrum.* **2012**, *83*, 125107. doi:10.1063/1.4770125.
95. Drewitt, J. W. E.; Emmens, B.; Kong, Z.-H.; Drinkwater, B. W.; Barnes, A. C. MightyLev: An Acoustic Levitator for High-Temperature Containerless Processing of Medium- to High-Density Materials. *Rev. Sci. Instrum.* **2024**, *95*, doi:10.1063/5.0221899.
96. Gangopadhyay, A. K.; Sellers, M. E.; Bracker, G. P.; Holland-Moritz, D.; Van Hoesen, D. C.; Koch, S.; Galenko, P. K.; Pauls, A. K.; Hyers, R. W.; Kelton, K. F. Demonstration of the Effect of Stirring on Nucleation from Experiments on the International Space Station Using the ISS-EML Facility. *NPJ Microgravity.* **2021**, *7*, 31. doi:10.1038/s41526-021-00161-9.
97. Alderman, O.; Lazareva, L.; Wilding, M.; Benmore, C.; Heald, S.; Johnson, C.; Johnson, J.; Hah, H.-Y.; Sendelbach, S.; Tamalonis, A.; et al. Local Structural Variation with Oxygen Fugacity in Fe_2SiO_{4+x} Fayalitic Iron Silicate Melts. *Geochim. Cosmochim. Acta* **2017**, *203*, 15–36. doi:10.1016/j.gca.2016.12.038.
98. Egry, I.; Lohöfer, G.; Seyhan, I.; Schneider, S.; Feuerbacher, B. Viscosity and Surface Tension Measurements in Microgravity. *Int. J. Thermophys.* **1999**, *20*, 1005. doi:10.1023/A:1022686316437.
99. Lohöfer, G.; Piller, J. The New ISS Electromagnetic Levitation Facility: MSL-EML. In *40th AIAA Aerospace Sciences Meeting & Exhibit*. American Institute of Aeronautics and Astronautics: Reston, Virigina, **2002**. doi:10.2514/6.2002-764.
100. Lohöfer, G. Electrical Resistivity Measurement of Liquid Metals. *Meas. Sci. Technol.* **2005**, *16*, 417–425. doi:10.1088/0957-0233/16/2/012.
101. Egry, I.; Lohöfer, G.; Matson, D. EML Processing Measurement Techniques. *High Temp. Mater. Process* **2008**, *27*, 389. doi:10.1515/HTMP.2008.27.6.389.
102. Mohr, M.; Hofmann, D. C.; Fecht, H.-J. Thermophysical Properties of an $Fe_{57.75}Ni_{19.25}Mo_{10}C_5B_8$ Glass-Forming Alloy Measured in Microgravity. *Adv. Eng. Mater* **2020**, *2001143*, 2001143. doi:10.1002/adem.202001143.
103. Wunderlich, R. K.; Fecht, H. J. Surface Tension and Viscosity of NiAl Catalytic Precursor Alloys from Microgravity Experiments. *Int. J. Mater. Res* **2011**, *102*, 1164–1173. doi:10.3139/146.110572.
104. Bracker, G.; Xiao, X.; Lee, J.; Reinartz, M.; Burggraf, S.; Herlach, D.; Rettenmayr, M.; Matson, D.; Hyers, R. Modeling of Fluid Flow Effects on Experiments Using Electromagnetic Levitation in Reduced Gravity. *Miner. Met. Mater. Ser.* **2019**, 171. doi:10.1007/978-3-030-05728-2_16.
105. Mohr, M.; Wunderlich, R. K.; Zweiacker, K.; Prades-Rödel, S.; Sauget, R.; Blatter, A.; Logé, R.; Dommann, A.; Neels, A.; Johnson, W. L.; Fecht, H.-J. Surface Tension and Viscosity of Liquid $Pd_{43}Cu_{27}Ni_{10}P_{20}$ Measured in a Levitation Device under Microgravity. *NPJ Microgravity.* **2019**, *5*, 4. doi:10.1038/s41526-019-0065-4.
106. Paradis, P.-F.; Rhim, W.-K. Thermophysical Properties of Zirconium at High Temperature. *J. Mater. Res.* **1999**, *14*, 3713–3719. doi:10.1557/JMR.1999.0501.
107. Egami, T.; Billinge, S. J. L. *Underneath the Bragg Peaks: Structural Analysis of Complex Materials*; Pergamon Press Ltd, **2003**.
108. Guo, G.-Q.; Wu, S.-Y.; Luo, S.; Yang, L. Detecting Structural Features in Metallic Glass via Synchrotron Radiation Experiments Combined with Simulations. *Metals* **2015**, *5*, 2093–2108. doi:10.3390/met5042093.
109. Akkerman, A. F.; Chernov, G. Y. Mean Free Paths by Inelastic Interactions, Stopping Powers, and Energy Straggling for Electrons of Energies up to 20 keV in Various Solids. *Phys. Status Solidi (b)* **1978**, *89*, 329–333. doi:10.1002/pssb.2220890142.
110. Akar, A.; Gümüş, H.; Okumuşoğlu, N. T. Electron Inelastic Mean Free Path Formula and CSDA-Range Calculation in Biological Compounds for Low and Intermediate Energies. *Appl. Radiat. Isot.* **2006**, *64*, 543–550. doi:10.1016/j.apradiso.2005.11.014.

111. Nunes, J. P.; Ledbetter, K.; Lin, M.; Kozina, M.; Deponte, D. P.; Biasin, E.; Centurion, M.; Crissman, C. J.; Dunning, M.; Guillet, S.; et al. Liquid-Phase Mega-Electron-Volt Ultrafast Electron Diffraction. *Struct. Dyn.* **2020**, *7*, 024301. doi:10.1063/1.5144518.
112. Kohara, S.; Ohara, K.; Tajiri, H.; Song, C.; Sakata, O.; Usuki, T.; Benino, Y.; Mizuno, A.; Masuno, A.; Okada, J. T.; et al. Synchrotron X-Ray Scattering Measurements of Disordered Materials. *Z. Phys. Chem.* **2016**, *230*, 339–368. doi:10.1515/zpch-2015-0654.
113. Willmott, P. An Introduction to Synchrotron Radiation. Wiley, **2019**. doi:10.1002/9781119280453.
114. Waseda, Y. Anomalous X-Ray Scattering for Material Characterization. In *Springer Tracts in Modern Physics*. Springer: Berlin, Heidelberg, **2002**; Vol. 179. doi:10.1007/3-540-46008-X.
115. Matsubara, E.; Sugiyama, K.; Shinohara, A.; Waseda, Y.; Inoue, A.; Zhang, T.; Masumoto, T. Structural Study of $Zr_{33}Y_{27}Al_{15}Ni_{25}$ Amorphous Alloys by Anomalous X-Ray Scattering (AXS). *Mater. Sci. Eng. A* **1994**, *179–180*, 444–447. doi:10.1016/0921-5093(94)90243-7.
116. Hosokawa, S.; Bérar, J.-F.; Boudet, N.; Ichitsubo, T.; Matsubara, E.; Pilgrim, W.-C.; Nishiyama, N. Partial Structure of $Pd_{42.5}Ni_{7.5}Cu_{30}P_{20}$ Bulk Metallic Glass: Comparison to the Reference $Pd_{40}Ni_{40}P_{20}$ Glass. *J. Phys.: Conf. Ser.* **2008**, *98*, 012013. doi:10.1088/1742-6596/98/1/012013.
117. Kohara, S.; Tajiri, H.; Song, C. H.; Ohara, K.; Temleitner, L.; Sugimito, K.; Fujiwara, A.; Pusztai, L.; Usuki, T.; Hosokawa, S.; et al. Anomalous x-Ray Scattering Studies of Functional Disordered Materials. *J. Phys: Conf. Ser.* **2014**, *502*, 012014. doi:10.1088/1742-6596/502/1/012014.
118. Kawamata, T.; Muto, T.; Sugiyama, K. Fine Structure of $Zr_{80}Pt_{20}$ Amorphous Alloy Determined from Anomalous X-Ray Scattering (AXS) Data by Applying Reverse Monte-Carlo (RMC) Simulation Method. *Mater. Trans.* **2021**, *62*, 20–26. doi:10.2320/matertrans.MT-M2020246.
119. Di Cicco, A. X-Ray Absorption Spectroscopy Investigations of Disordered Matter. *Radiat. Phys. Chem.* **2020**, *175*, 108077. doi:10.1016/j.radphyschem.2018.11.031.
120. Grünert, W.; Klementiev, K. X-Ray Absorption Spectroscopy Principles and Practical Use in Materials Analysis. *Phys. Sci. Rev* **2020**, *5*, 1. doi:10.1515/psr-2017-0181.
121. Buzanich, A. G.; Radtke, M.; Reinholz, U.; Riesemeier, H.; Emmerling, F. Time- and Spatial-Resolved XAFS Spectroscopy in a Single Shot: New Analytical Possibilities for in Situ Material Characterization. *J. Synchrotron Rad.* **2016**, *23*, 769–776. doi:10.1107/S1600577516003969.
122. Bornmann, B.; Kläs, J.; Müller, O.; Lützenkirchen-Hecht, D.; Frahm, R. The Quick EXAFS Setup at Beamline P64 at PETRA III for up to 200 Spectra per Second. *AIP Conf. Proc.* **2019**, *2054*, 040008. doi:10.1063/1.5084609.
123. Lee, P. A.; Citrin, P. H.; Eisenberger, P.; Kincaid, B. M. Extended x-Ray Absorption Fine Structure -Its Strengths and Limitations as a Structural Tool. *Rev. Mod. Phys.* **1981**, *53*, 769–806. doi:10.1103/RevModPhys.53.769.
124. Porro, M.; Andricek, L.; Bombelli, L.; De Vita, G.; Fiorini, C.; Fischer, P.; Hansen, K.; Lechner, P.; Lutz, G.; Strüder, L.; Weidenspointner, G. Expected Performance of the DEPFET Sensor with Signal Compression: A Large Format X-Ray Imager with Mega-Frame Readout Capability for the European XFEL. *Nucl. Instrum. Methods Phys. Res. Sect. A Accel. Spectrometers, Detect. Assoc. Equip* **2010**, *624*, 509–519. doi:10.1016/j.nima.2010.02.254.
125. Zalden, P.; Quirin, F.; Schumacher, M.; Siegel, J.; Wei, S.; Koc, A.; Nicoul, M.; Trigo, M.; Andreasson, P.; Enquist, H.; et al. Femtosecond x-Ray Diffraction Reveals a Liquid–Liquid Phase Transition in Phase-Change Materials. *Science* **2019**, *364*, 1062–1067. doi:10.1126/science.aaw1773.
126. Antonowicz, J.; Olczak, A.; Sokolowski-Tinten, K.; Zalden, P.; Milov, I.; Dzięgielewski, P.; Bressler, C.; Chapman, H. N.; Chojnacki, M.; Dłużewski, P.; et al. Structural Pathways for Ultrafast Melting of Optically Excited Thin Polycrystalline Palladium Films. *Acta Mater.* **2024**, *276*, 120043. doi:10.1016/j.actamat.2024.120043.
127. McGreevy, R. L. Reverse Monte Carlo Modelling. *J. Phys: Condens. Matter.* **2001**, *13*, R877–R913. doi:10.1088/0953-8984/13/46/201.
128. Nosé, S. A Molecular Dynamics Method for Simulations in the Canonical Ensemble. *Mol. Phys.* **1984**, *52*, 255–268. doi:10.1080/00268978400101201.
129. Plimpton, S. Fast Parallel Algorithms for Short-Range Molecular Dynamics. *J. Comput. Phys.* **1995**, *117*, 1–19. doi:10.1006/jcph.1995.1039.
130. Kresse, G.; Hafner, J. Ab Initio Molecular Dynamics for Liquid Metals. *Phys. Rev. B Condens. Matter.* **1993**, *47*, 558–561. doi:10.1103/PhysRevB.47.558.
131. Sinha, S.; Srivastava, P. L.; Singh, R. N. Temperature-Dependent Structure and Electrical Transport in Liquid Metals. *J. Phys: Condens. Matter.* **1989**, *1*, 1695–1705. doi:10.1088/0953-8984/1/9/014.
132. Faber, T. E.; Ziman, J. M. A Theory of the Electrical Properties of Liquid Metals III. The Resistivity of Binary Alloys. *Philos. Mag.* **1965**, *11*, 153–173. doi:10.1080/14786436508211931.
133. Häussler, P. Interrelations between Atomic and Electronic Structures - Liquid and Amorphous Metals as Model Systems. *Phys. Rep.* **1992**, *222*, 65–143. doi:10.1016/0370-1573(92)90018-U.
134. Stiehler, M. E.; Jolly, M. R.; Georgarakis, K. On the Impact of Global Interactions on the Structure of Metallic Glasses. *J. Alloy. Compd.* **2019**, *782*, 496–505. doi:10.1016/j.jallcom.2018.12.086.
135. Basham, M.; Filik, J.; Wharmby, M. T.; Chang, P. C. Y.; El Kassaby, B.; Gerring, M.; Aishima, J.; Levik, K.; Pulford, B. C. A.; Sikharulidze, I.; et al. Data Analysis WorkbeNch (DAWN). *J. Synchrotron Radiat.* **2015**, *22*, 853–858. doi:10.1107/S1600577515002283.
136. Filik, J.; Ashton, A. W.; Chang, P. C. Y.; Chater, P. A.; Day, S. J.; Drakopoulos, M.; Gerring, M. W.; Hart, M. L.; Magdysyuk, O. V.; Michalik, S.; et al.

Processing Two-Dimensional X-Ray Diffraction and Small-Angle Scattering Data in DAWN 2. *J. Appl. Crystallogr.* **2017**, *50*, 959–966. doi:10.1107/S1600576717004708.

137. Hammersley, A. P.; Svensson, S. O.; Hanfland, M.; Fitch, A. N.; Hausermann, D. Two-Dimensional Detector Software: From Real Detector to Idealised Image or Two-Theta Scan. *High Press. Res.* **1996**, *14*, 235–248. doi:10.1080/08957959608201408.
138. Krogh-Moe, J. A Method for Converting Experimental X-Ray Intensities to an Absolute Scale. *Acta Cryst.* **1956**, *9*, 951–953. doi:10.1107/S0365110X56002655.
139. Norman, N. The Fourier Transform Method for Normalizing Intensities. *Acta Cryst.* **1957**, *10*, 370–373. doi:10.1107/S0365110X57001085.
140. Soper, A. K. GudrunN and GudrunX: Programs for Correcting Raw Neutron and X-Ray Diffraction Data to Differential Scattering Cross Section. In *Rutherford Appleton Laboratory Technical Report RAL-TR-2011-013*; Science and Technology Facilities Council, Didcot, **2011**.
141. Soper, A. K.; Barney, E. R. On the Use of Modification Functions When Fourier Transforming Total Scattering Data. *J. Appl. Crystallogr.* **2012**, *45*, 1314–1317. doi:10.1107/S002188981203960X.
142. Juhás, P.; Davis, T.; Farrow, C. L.; Billinge, S. J. PDFgetX3: A Rapid and Highly Automatable Program for Processing Powder Diffraction Data into Total Scattering Pair Distribution Functions. *J. Appl. Crystallogr.* **2013**, *46*, 560–566. doi:10.1107/S0021889813005190.
143. Tucker, M. G.; Keen, D. A.; Dove, M. T.; Goodwin, A. L.; Hui, Q. RMCProfile: Reverse Monte Carlo for Polycrystalline Materials. *J. Phys. Condens. Matter.* **2007**, *19*, 335218. doi:10.1088/0953-8984/19/33/335218.
144. Gereben, O.; Jóvári, P.; Temleitner, L.; Pusztai, L. A New Version of the RMC++ Reverse Monte Carlo Programme, Aimed at Investigating the Structure of Covalent Glasses. *J. Optoelectron. Adv. Mater.* **2007**, *9*, 3021.
145. Sánchez-Portal, D.; Ordejón, P.; Artacho, E.; Soler, J. M. Density-Functional Method for Very Large Systems with LCAO Basis Sets. *Int. J. Quantum Chem.* **1997**, *65*, 453. doi:10.1002/(SICI)1097-461X(1997)65:5.
146. Artacho, E.; Sánchez-Portal, D.; Ordejón, P.; Garcia, A.; Soler, J. M. Linear-Scaling ab-Initio Calculations for Large and Complex Systems. *Phys. Stat. Sol. (b)* **1999**, *215*, 809–817. doi:10.1002/(SICI)1521-3951(199909)215:1. 10.1002/(SICI)1521-3951(199909)215:1<809::AID-PSSB809>3.0.CO;2-0
147. Soler, J. M.; Artacho, E.; Gale, J. D.; García, A.; Junquera, J.; Ordejón, P.; Sánchez-Portal, D. The SIESTA Method for ab Initio order-N Materials Simulation. *J. Phys: Condens. Matter* **2002**, *14*, 2745–2779. doi:10.1088/0953-8984/14/11/302.
148. Kim, Y. J.; Busch, R.; Johnson, W. L.; Rulison, A. J.; Rhim, W. K. Experimental Determination of a Time–Temperature-Transformation Diagram of the Undercooled $Zr_{41.2}Ti_{13.8}Cu_{12.5}Ni_{10.0}Be_{22.5}$ Alloy Using the Containerless Electrostatic Levitation Processing Technique. *Appl. Phys. Lett.* **1996**, *68*, 1057–1059. doi:10.1063/1.116247.
149. Louzguine-Luzgin, D. V.; Belosludov, R.; Yavari, A. R.; Georgarakis, K.; Vaughan, G.; Kawazoe, Y.; Egami, T.; Inoue, A. Structural Basis for Supercooled Liquid Fragility Established by Synchrotron-Radiation Method and Computer Simulation. *J. Appl. Phys.* **2011**, *110*, 043519. doi:10.1063/1.3624745.
150. Stiehler, M. E.; Panagiotopoulos, N. T.; Keeble, D. S.; Ivanov, Y. P.; Menelaou, M.; Jolly, M. R.; Greer, A. L.; Georgarakis, K. The Effect of Ni or Co Additions on the Structure of $Zr_{60}Cu_{30}Al_{10}$ Bulk Metallic Glass Revealed by High-Energy Synchrotron Radiation. *Mater. Today Commun.* **2022**, *31*, 103531. doi:10.1016/j.mtcomm.2022.103531.
151. McGreevy, R. L.; Baranyai, A.; Ruff, I. A Less Arbitrary Determination of Coordination Numbers in Disordered Systems. *Phys. Chem. Liq.* **1986**, *16*, 47–54. doi:10.1080/00319108608078499.
152. del Rio, B. G.; González, L. E.; González, D. J. First Principles Study of Liquid Uranium at Temperatures up to 2050 K. *J. Phys. Condens. Matter.* **2020**, *32*, 304001. doi:10.1088/1361-648X/ab7f6f.
153. Georgarakis, K.; Louzguine-Luzgin, D. V.; Antonowicz, J.; Vaughan, G.; Yavari, A. R.; Egami, T.; Inoue, A. Variations in Atomic Structural Features of a Supercooled Pd-Ni-Cu-P Glass Forming Liquid During *In Situ* Vitrification. *Acta Mater.* **2011**, *59*, 708–716. doi:10.1016/j.actamat.2010.10.009.
154. Ryu, C. W.; Dmowski, W.; Egami, T. Ideality of Liquid Structure: A Case Study for Metallic Alloy Liquids. *Phys. Rev. E* **2020**, *101*, 030601. doi:10.1103/PhysRevE.101.030601.
155. Ding, J.; Xu, M.; Guan, P. F.; Deng, S. W.; Cheng, Y. Q.; Ma, E. Temperature Effects on Atomic Pair Distribution Functions of Melts. *J. Chem. Phys.* **2014**, *140*, 064501. doi:10.1063/1.4864106.
156. Dong, W.; Wu, Z.; Ge, J.; Liu, S.; Lan, S.; Gilbert, E. P.; Ren, Y.; Ma, D.; Wang, X.-L. In Situ Neutron Scattering Studies of a Liquid-Liquid Phase Transition in the Supercooled Liquid of a Zr-Cu-Al-Ag Glass-Forming Alloy. *Appl. Phys. Lett.* **2021**, *118*, 191901. doi:10.1063/5.0048486.
157. Debenedetti, P. G.; Stillinger, F. H. Supercooled Liquids and the Glass Transition. *Nature* **2001**, *410*, 259–267. doi:10.1038/35065704.
158. Mukherjee, S.; Zhou, Z.; Schroers, J.; Johnson, W. L.; Rhim, W. K. Overheating Threshold and Its Effect on Time-Temperature-Transformation Diagrams of Zirconium Based Bulk Metallic Glasses. *Appl. Phys. Lett.* **2004**, *84*, 5010–5012. doi:10.1063/1.1763219.
159. Mauro, N. A.; Johnson, M. L.; Bendert, J. C.; Kelton, K. F. Structural Evolution in Ni-Nb and Ni-Nb-Ta Liquids and glasses - A Measure of Liquid Fragility? *J. Non-Cryst. Solids* **2013**, *362*, 237. doi:10.1016/j.jnoncrysol.2012.11.022.
160. Mauro, N. A.; Vogt, A. J.; Johnson, M. L.; Bendert, J. C.; Kelton, K. F. Anomalous Structural Evolution

in $Cu_{50}Zr_{50}$ Glass-Forming Liquids. *Appl. Phys. Lett.* **2013**, *103*, 021904. doi:10.1063/1.4813389.
161. Mauro, N. A.; Blodgett, M.; Johnson, M. L.; Vogt, A. J.; Kelton, K. F. A Structural Signature of Liquid Fragility. *Nat. Commun.* **2014**, *5*, 4616. doi:10.1038/ncomms5616.
162. Ashcroft, N. W.; Mermin, N. D. *Solid State Physics*; Saunders College Publishing: Philadelphia, **1976**.
163. Jonas, I.; Yang, F.; Meyer, A. Long-Range Mass Transport During Structural Transitions in Metallic Glass-Forming Melts. *Phys. Rev. Lett.* **2019**, *123*, 055502. doi:10.1103/PhysRevLett.123.055502.
164. Mattern, N. Structure Formation in Liquid and Amorphous Metallic Alloys. *J. Non-Cryst. Solids* **2007**, *353*, 1723–1731. doi:10.1016/j.jnoncrysol.2007.01.042.
165. Cheng, Y. Q.; Ma, E.; Sheng, H. W. Alloying Strongly Influences the Structure, Dynamics, and Glass Forming Ability of Metallic Supercooled Liquids. *Appl. Phys. Lett.* **2008**, *93*, 111913. doi:10.1063/1.2987727.
166. Cheng, Y. Q.; Ma, E.; Sheng, H. W. Atomic Level Structure in Multicomponent Bulk Metallic Glass. *Phys. Rev. Lett.* **2009**, *102*, 245501. doi:10.1103/PhysRevLett.102.245501.
167. Soklaski, R.; Nussinov, Z.; Markow, Z.; Kelton, K. F.; Yang, L. Connectivity of Icosahedral Network and a Dramatically Growing Static Length Scale in Cu-Zr Binary Metallic Glasses. *Phys. Rev. B.* **2013**, *87*, 184203. doi:10.1103/PhysRevB.87.184203.
168. Stepanyuk, V.; Szasz, A.; Katsnelson, A.; Trushin, O.; Müller, H.; Kirchmayr, H. Microstructure and Its Relaxation in Fe-B Amorphous System Simulated by Molecular Dynamics. *J. Non-Cryst. Solids* **1993**, *159*, 80–87. doi:10.1016/0022-3093(93)91284-A.
169. Ma, E. Tuning Order in Disorder. *Nat. Mater.* **2015**, *14*, 547–552. doi:10.1038/nmat4300.
170. Zhang, Y.; Mattern, N.; Eckert, J. Atomic Structure and Transport Properties of $Cu_{50}Zr_{45}Al_5$ Metallic Liquids and Glasses: Molecular Dynamics Simulations. *J. Appl. Phys.* **2011**, *110*, 093506. doi:10.1063/1.3658252.
171. Cheng, Y.; Ma, E. Atomic-Level Structure and Structure-Property Relationship in Metallic Glasses. *Prog. Mater. Sci.* **2011**, *56*, 379–473. doi:10.1016/j.pmatsci.2010.12.002.
172. Cheng, Y.; Cao, A.; Ma, E. Correlation Between the Elastic Modulus and the Intrinsic Plastic Behavior of Metallic Glasses: The Roles of Atomic Configuration and Alloy Composition. *Acta Mater.* **2009**, *57*, 3253–3267. doi:10.1016/j.actamat.2009.03.027.
173. Frank, F. C. Supercooling of Liquids. *Proc. R. Soc. London. Ser. A. Math. Phys. Sci.* **1952**, *215*, 43. doi:10.1098/rspa.1952.0194.
174. Lekka, C.; Evangelakis, G. Bonding Characteristics and Strengthening of CuZr Fundamental Clusters upon Small Al Additions from Density Functional Theory Calculations. *Scr. Mater.* **2009**, *61*, 974–977. doi:10.1016/j.scriptamat.2009.08.008.
175. Kaban, I.; Jóvári, P.; Kokotin, V.; Shuleshova, O.; Beuneu, B.; Saksl, K.; Mattern, N.; Eckert, J.; Greer, A. Local Atomic Arrangements and Their Topology in Ni-Zr and Cu-Zr Glassy and Crystalline Alloys. *Acta Mater.* **2013**, *61*, 2509–2520. doi:10.1016/j.actamat.2013.01.027.
176. Inoue, A.; Negishi, T.; Kimura, H. M.; Zhang, T.; Yavari, A. R. High Packing Density of Zr- and Pd-Based Bulk Amorphous Alloys. *Mater. Trans, JIM* **1998**, *39*, 318–321. doi:10.2320/matertrans1989.39.318.
177. Gangopadhyay, A. K.; Blodgett, M. E.; Johnson, M. L.; McKnight, J.; Wessels, V.; Vogt, A. J.; Mauro, N. A.; Bendert, J. C.; Soklaski, R.; Yang, L.; Kelton, K. F. Anomalous Thermal Contraction of the First Coordination Shell in Metallic Alloy Liquids. *J. Chem. Phys.* **2014**, *140*, 044505. doi:10.1063/1.4861666.
178. Lou, H.; Wang, X.; Cao, Q.; Zhang, D.; Zhang, J.; Hu, T.; Mao, H.-K.; Jiang, J.-Z. Negative Expansions of Interatomic Distances in Metallic Melts. *Proc. Natl. Acad. Sci. U S A* **2013**, *110*, 10068–10072. doi:10.1073/pnas.1307967110.
179. Cargill, G. Structure of Metallic Alloy Glasses. In *Solid State Physics. Advances in Research and Application*. Ehrenreich, H., Seitz, F., Turnbull, D., Eds.; Academic Press, **1975**; Vol. 30, pp. 227–320. doi:10.1016/S0081-1947(08)60337-9.
180. Ryu, C. W.; Egami, T. Medium-Range Atomic Correlation in Simple Liquids. I. Distinction from Short-Range Order. *Phys. Rev. E* **2021**, *104*, 064109. doi:10.1103/PhysRevE.104.064109.
181. Häussler, P.; Barzola-Quiquia, J.; Hauschild, D.; Rauchhaupt, J.; Stiehler, M.; Hackert, M. Spherical Periodicity, a General Feature of Matter at Its Early Stages of Formation. In *TMS Annual Meeting, The Minerals, Metals and Materials Society*; Massalski, T. B., Turchi, P., Eds.; The Minerals, Metals and Materials Society, Wiley: New York, **2005**; pp. 43–86.
182. Ali Khan, S.; Wang, X.-D.; Saeed Ahmad, A.; Cao, Q.-P.; Zhang, D.-X.; Fang, Y.-Z.; Wang, H.; Jiang, J.-Z. Temperature- and Pressure-Induced Polyamorphic Transitions in AuCuSi Alloy. *J. Phys. Chem. C* **2019**, *123*, 20342–20350. doi:10.1021/acs.jpcc.9b05167.
183. Lan, S.; Ren, Y.; Wei, X. Y.; Wang, B.; Gilbert, E. P.; Shibayama, T.; Watanabe, S.; Ohnuma, M.; Wang, X. L. Hidden Amorphous Phase and Reentrant Supercooled Liquid in Pd-Ni-P Metallic Glasses. *Nat. Commun.* **2017**, *8*, 14679. doi:10.1038/ncomms14679.
184. Shen, J.; Lu, Z.; Wang, J. Q.; Lan, S.; Zhang, F.; Hirata, A.; Chen, M. W.; Wang, X. L.; Wen, P.; Sun, Y. H.; et al. Metallic Glacial Glass Formation by a First-Order Liquid-Liquid Transition. *J. Phys. Chem. Lett.* **2020**, *11*, 6718–6723. doi:10.1021/acs.jpclett.0c01789.
185. McMillan, P. F.; Wilson, M.; Wilding, M. C.; Daisenberger, D.; Mezouar, M.; Neville Greaves, G. Polyamorphism and Liquid-Liquid Phase Transitions: Challenges for Experiment and Theory. *J. Phys. Condens. Matter.* **2007**, *19*, 415101. doi:10.1088/0953-8984/19/41/415101.
186. Soklaski, R.; Tran, V.; Nussinov, Z.; Kelton, K. F.; Yang, L. A Locally Preferred Structure Characterises All Dynamical Regimes of a Supercooled Liquid.

Philos. Mag. **2016**, *96*, 1212–1227. doi:10.1080/14786435.2016.1158427.
187. Lad, K. N.; Jakse, N.; Pasturel, A. Signatures of Fragile-to-Strong Transition in a Binary Metallic Glass-Forming Liquid. *J. Chem. Phys.* **2012**, *136*, 104509. doi:10.1063/1.3692610.
188. Zhou, C.; Hu, L.; Sun, Q.; Zheng, H.; Zhang, C.; Yue, Y. Structural Evolution during Fragile-to-Strong Transition in CuZr(Al) Glass-Forming Liquids. *J. Chem. Phys.* **2015**, *142*, 064508. doi:10.1063/1.4907374.
189. Wang, C. C.; Wong, C. H. Interpenetrating Networks in Zr-Cu-Al and Zr-Cu Metallic Glasses. *Intermetallics* **2012**, *22*, 13–16. doi:10.1016/j.intermet.2011.10.022.
190. Angell, C. A. Glass Formation and Glass Transition in Supercooled Liquids, with Insights from Study of Related Phenomena in Crystals. *J. Non-Cryst. Solids* **2008**, *354*, 4703–4712. doi:10.1016/j.jnoncrysol.2008.05.054.
191. Xu, L.; Buldyrev, S. V.; Giovambattista, N.; Angell, C. A.; Stanley, H. E. A Monatomic System with a Liquid-Liquid Critical Point and Two Distinct Glassy States. *J. Chem. Phys.* **2009**, *130*, 054505. doi:10.1063/1.3043665.
192. Janssen, L. M. C. Mode-Coupling Theory of the Glass Transition: A Primer. *Front. Phys.* **2018**, *6*, 1. doi:10.3389/fphy.2018.00097.
193. Egami, T.; Ryu, C. W. Why Is the Range of Timescale So Wide in Glass-Forming Liquid? *Front. Chem.* **2020**, *8*, 579169. doi:10.3389/fchem.2020.579169.
194. Sheng, H. W.; Ma, E.; Kramer, M. J. Relating Dynamic Properties to Atomic Structure in Metallic Glasses. *JOM* **2012**, *64*, 856–881. doi:10.1007/s11837-012-0360-y.
195. Adam, G.; Gibbs, J. H. On the Temperature Dependence of Cooperative Relaxation Properties in Glass-Forming Liquids. *J. Chem. Phys.* **1965**, *43*, 139–146. doi:10.1063/1.1696442.
196. Stevenson, J. D.; Schmalian, J.; Wolynes, P. G. The Shapes of Cooperatively Rearranging Regions in Glass-Forming Liquids. *Nature Phys.* **2006**, *2*, 268–274. doi:10.1038/nphys261.
197. Gangopadhyay, A. K.; Kelton, K. F. Recent Progress in Understanding High Temperature Dynamical Properties and Fragility in Metallic Liquids, and Their Connection with Atomic Structure. *J. Mater. Res.* **2017**, *32*, 2638–2657. doi:10.1557/jmr.2017.253.
198. Zheng, N.; Wang, G.; Zhang, L.; Calin, M.; Stoica, M.; Vaughan, G.; Mattern, N.; Eckert, J. In Situ High-Energy x-Ray Diffraction Observation of Structural Evolution in a Ti-Based Bulk Metallic Glass upon Heating. *J. Mater. Res.* **2010**, *25*, 2271–2277. doi:10.1557/jmr.2010.0298.
199. Calin, M.; Stoica, M.; Zheng, N.; Wang, X. R.; Scudino, S.; Gebert, A.; Eckert, J. Thermal Stability and Crystallization Kinetics of $Ti_{40}Zr_{10}Cu_{34}Pd_{14}Sn_2$ Bulk Metallic Glass. *SSP.* **2012**, *188*, 3–10. doi:10.4028/www.scientific.net/SSP.188.3.
200. Chen, E.-Y.; Peng, S.-X.; Peng, L.; Michiel, M. D.; Vaughan, G. B.; Yu, Y.; Yu, H.-B.; Ruta, B.; Wei, S.; Liu, L. Glass-Forming Ability Correlated with the Liquid-Liquid Transition in $Pd_{42.5}Ni_{42.5}P_{15}$ Alloy. *Scr. Mater.* **2021**, *193*, 117. doi:10.1016/j.scriptamat.2020.10.042.
201. An, Q.; Johnson, W. L.; Samwer, K.; Corona, S. L.; Goddard, W. A. Formation of Two Glass Phases in Binary Cu-Ag Liquid. *Acta Mater.* **2020**, *195*, 274–281. doi:10.1016/j.actamat.2020.05.060.
202. An, Q.; Johnson, W. L.; Samwer, K.; Corona, S. L.; Goddard, W. A. First-Order Phase Transition in Liquid Ag to the Heterogeneous G-Phase. *J. Phys. Chem. Lett.* **2020**, *11*, 632–645. doi:10.1021/acs.jpclett.9b03699.
203. Na, J. H.; Corona, S. L.; Hoff, A.; Johnson, W. L. Observation of an Apparent First-Order Glass Transition in Ultrafragile Pt-Cu-P Bulk Metallic Glasses. *Proc. Natl. Acad. Sci. U S A* **2020**, *117*, 2779–2787. doi:10.1073/pnas.1916371117.
204. An, Q.; Johnson, W. L.; Samwer, K.; Corona, S. L.; Goddard, W. A. The First Order L-G Phase Transition in Liquid Ag and Ag-Cu Alloys is Driven by Deviatoric Strain. *Scr. Mater.* **2021**, *194*, 113695. doi:10.1016/j.scriptamat.2020.113695.
205. Khalouk, K.; Mayoufi, M.; Gasser, J. G. Are There Phase Transitions in Liquid Metallic Alloys? *Philos. Mag.* **2010**, *90*, 2695–2709. doi:10.1080/14786431003745310.
206. He, Y.; Li, J.; Li, L.; Wang, J.; Yildiz, E.; Beaugnon, E. Composition Dependent Characteristic Transition Temperatures of Co-B Melts. *J. Non-Cryst. Solids* **2019**, *522*, 119583. doi:10.1016/j.jnoncrysol.2019.119583.
207. Lin, H.-J.; He, M.; Pan, S.-P.; Gu, L.; Li, H.-W.; Wang, H.; Ouyang, L.-Z.; Liu, J.-W.; Ge, T.-P.; Wang, D.-P.; et al. Towards Easily Tunable Hydrogen Storage via a Hydrogen-Induced Glass-to-Glass Transition in Mg-Based Metallic Glasses. *Acta Mater.* **2016**, *120*, 68–74. doi:10.1016/j.actamat.2016.08.020.
208. Li, Y.; Georgarakis, K.; Pang, S.; Ma, C.; Vaughan, G.; Yavari, A. R.; Zhang, T. Real Time Synchrotron Radiation Studies on Metallic Glass $(Zr_{0.55}Al_{0.1}Ni_{0.05}Cu_{0.3})_{99}Y_1$ after Cold Rolling. *Intermetallics* **2009**, *17*, 231–234. doi:10.1016/j.intermet.2008.08.015.
209. Pineda, E.; Hidalgo, I.; Bruna, P.; Pradell, T.; Labrador, A.; Crespo, D. Structural Study of Conventional and Bulk Metallic Glasses during Annealing. *J. Alloy. Compd.* **2009**, *483*, 578–581. doi:10.1016/j.jallcom.2008.07.194.
210. Evertz, S.; Music, D.; Schnabel, V.; Bednarcik, J.; Schneider, J. M. Thermal Expansion of Pd-Based Metallic Glasses by ab Initio Methods and High Energy X-Ray Diffraction. *Sci. Rep.* **2017**, *7*, 15744. doi:10.1038/s41598-017-16117-7.
211. Botta, W. J.; Ota, K.; Hajlaoui, K.; Vaughan, G.; Yavari, A. R. Glass Transition, Thermal Expansion and Relaxation in B_2O_3 Glass Measured by Time-Resolved X-Ray Diffraction. *J. Non-Cryst. Solids* **2008**, *354*, 325–327. doi:10.1016/j.jnoncrysol.2007.07.043.

212. Drewitt, J. W. E.; Jahn, S.; Hennet, L. Configurational Constraints on Glass Formation in the Liquid Calcium Aluminate System. *J. Stat. Mech.* **2019**, *2019*, 104012. doi:10.1088/1742-5468/ab47fc.
213. Mendelev, M. I.; Kramer, M. J.; Ott, R. T.; Sordelet, D. J.; Besser, M. F.; Kreyssig, A.; Goldman, A. I.; Wessels, V.; Sahu, K. K.; Kelton, K. F.; et al. Experimental and Computer Simulation Determination of the Structural Changes Occurring Through the Liquid-Glass Transition in Cu-Zr Alloys. *Philos. Mag.* **2010**, *90*, 3795–3815. doi:10.1080/14786435.2010.494585.
214. Georgarakis, K.; Yavari, A. R.; Louzguine-Luzgin, D. V.; Antonowicz, J.; Stoica, M.; Li, Y.; Satta, M.; LeMoulec, A.; Vaughan, G.; Inoue, A. Atomic Structure of Zr-Cu Glassy Alloys and Detection of Deviations from Ideal Solution Behavior with Al Addition by x-Ray Diffraction Using Synchrotron Light in Transmission. *Appl. Phys. Lett.* **2009**, *94*, 48. doi:10.1063/1.3136428.
215. Angell, C. A.; Ngai, K. L.; McKenna, G. B.; McMillan, P. F.; Martin, S. W. Relaxation in Glassforming Liquids and Amorphous Solids. *J. Appl. Phys.* **2000**, *88*, 3113–3157. doi:10.1063/1.1286035.
216. Egami, T. Local Density Correlations in Liquids. *Front. Phys.* **2020**, *8*, 1. doi:10.3389/fphy.2020.00050.
217. Bellazzini, R.; Spandre, G.; Brez, A.; Minuti, M.; Pinchera, M.; Mozzo, P. Chromatic X-Ray Imaging with a Fine Pitch CdTe Sensor Coupled to a Large Area Photon Counting Pixel ASIC. *J. Inst.* **2013**, *8*, C02028–C02028. doi:10.1088/1748-0221/8/02/C02028.
218. Bellazzini, R.; Brez, A.; Spandre, G.; Minuti, M.; Pinchera, M.; Delogu, P.; De Ruvo, P. L.; Vincenzi, A. PIXIE III: A Very Large Area Photon-Counting CMOS Pixel ASIC for Sharp X-Ray Spectral Imaging. *J. Inst.* **2015**, *10*, C01032–C01032. doi:10.1088/1748-0221/10/01/C01032.
219. Mokso, R.; Oberta, P. Simultaneous Dual-Energy X-Ray Stereo Imaging. *J. Synchrotron Radiat.* **2015**, *22*, 1078–1082. doi:10.1107/S1600577515006554.
220. Hrdý, J.; Hrdá, J.; Oberta, P.; Pacherová, O. Two (and More) Sharp X-Ray Wavelengths in One Beam. *Nucl. Instrum. Methods Phys. Res. Sect. A Accel. Spectrometers, Detect. Assoc. Equip.* **2016**, *807*, 61–63. doi:10.1016/j.nima.2015.10.094.
221. Brun, F.; Di Trapani, V.; Batey, D.; Cipiccia, S.; Rau, C. Edge-Subtraction X-Ray Ptychographic Imaging with Pink Beam Synchrotron Radiation and a Single Photon-Counting Detector. *Sci. Rep.* **2020**, *10*, 6526. doi:10.1038/s41598-020-63161-x.
222. Cipiccia, S.; Brun, F.; Di Trapani, V.; Rau, C.; Batey, D. J. Dual Energy X-Ray Beam Ptycho-Fluorescence Imaging. *J. Synchrotron Radiat.* **2021**, *28*, 1916–1920. doi:10.1107/S1600577521008675.
223. Bras, W.; Dolbnya, I. P.; Detollenaere, D.; Van Tol, R.; Malfois, M.; Greaves, G. N.; Ryan, A. J.; Heeley, E. Recent Experiments on a Combined Small-Angle/Wide-Angle X-Ray Scattering Beam Line at the ESRF. *J. Appl. Crystallogr.* **2003**, *36*, 791–794. doi:10.1107/S002188980300400X.
224. Jaroszynski, D.; Bingham, R.; Brunetti, E.; Ersfeld, B.; Gallacher, J.; van der Geer, B.; Issac, R.; Jamison, S.; Jones, D.; de Loos, M.; et al. Radiation Sources Based on Laser–Plasma Interactions. *Philos. Trans. A Math. Phys. Eng. Sci.* **2006**, *364*, 689–710. doi:10.1098/rsta.2005.1732.
225. Schlenvoigt, H.-P.; Haupt, K.; Debus, A.; Budde, F.; Jäckel, O.; Pfotenhauer, S.; Schwoerer, H.; Rohwer, E.; Gallacher, J. G.; Brunetti, E.; et al. A Compact Synchrotron Radiation Source Driven by a Laser-Plasma Wakefield Accelerator. *Nat. Phys.* **2008**, *4*, 130–133. doi:10.1038/nphys811.
226. Couprie, M. E. Towards Compact Free Electron-Laser Based on Laser Plasma Accelerators. *Nucl. Instrum. Methods Phys. Res. Sect. A Accel. Spectrometers, Detect. Assoc. Equip.* **2018**, *909*, 5. doi:10.1016/j.nima.2018.02.090.
227. Feist, A.; Bach, N.; Rubiano da Silva, N.; Danz, T.; Möller, M.; Priebe, K. E.; Domröse, T.; Gatzmann, J. G.; Rost, S.; Schauss, J.; et al. Ultrafast Transmission Electron Microscopy Using a Laser-Driven Field Emitter: Femtosecond Resolution with a High Coherence Electron Beam. *Ultramicroscopy* **2017**, *176*, 63–73. doi:10.1016/j.ultramic.2016.12.005.
228. Lee, Y.; Oang, K. Y.; Kim, D.; Ihee, H. A Comparative Review of Time-Resolved x-Ray and Electron Scattering to Probe Structural Dynamics. *Struct. Dyn.* **2024**, *11*, 031301. doi:10.1063/4.0000249.
229. Weathersby, S. P.; Brown, G.; Centurion, M.; Chase, T. F.; Coffee, R.; Corbett, J.; Eichner, J. P.; Frisch, J. C.; Fry, A. R.; Gühr, M.; et al. Mega-Electron-Volt Ultrafast Electron Diffraction at SLAC National Accelerator Laboratory. *Rev. Sci. Instrum.* **2015**, *86*, 073702. doi:10.1063/1.4926994.
230. Zhong, L.; Wang, J.; Sheng, H.; Zhang, Z.; Mao, S. X. Formation of Monatomic Metallic Glasses through Ultrafast Liquid Quenching. *Nature* **2014**, *512*, 177–180. doi:10.1038/nature13617.
231. Tong, X.; Zhang, Y.-E.; Shang, B.; Zhang, H.-P.; Li, Z.; Zhang, Y.; Wang, G.; Liu, Y.; Zhao, Y.; Zhang, B.; et al. Breaking the Vitrification Limitation of Monatomic Metals. *Nat. Mater.* **2024**, *23*, 1193–1199. doi:10.1038/s41563-024-01967-0.
232. Hart, J. L.; Lang, A. C.; Leff, A. C.; Longo, P.; Trevor, C.; Twesten, R. D.; Taheri, M. L. Direct Detection Electron Energy-Loss Spectroscopy: A Method to Push the Limits of Resolution and Sensitivity. *Sci. Rep.* **2017**, *7*, 8243. doi:10.1038/s41598-017-07709-4.
233. Maigné, A.; Wolf, M. Low-Dose Electron Energy-Loss Spectroscopy Using Electron Counting Direct Detectors. *Microscopy (Oxf)* **2018**, *67*, i86–i97. doi:10.1093/jmicro/dfx088.
234. Vecchione, T.; Denes, P.; Jobe, R. K.; Johnson, I. J.; Joseph, J. M.; Li, R. K.; Perazzo, A.; Shen, X.; Wang, X. J.; Weathersby, S. P.; et al. A Direct Electron Detector for Time-Resolved MeV Electron Microscopy. *Rev. Sci. Instrum.* **2017**, *88*, 033702. doi:10.1063/1.4977923.
235. Maclaren, I.; Cummings, R. B.; Gordon, F.; Frutos-Myro, E.; McFadzean, S.; Brown, A. P.; Craven, A. J. *Performing EELS at Higher Energy Losses at Both 80*

and 200 kV. Elsevier Inc., Elsevier: Amsterdam, **2019**; Vol. 210. doi:10.1016/bs.aiep.2019.02.001.
236. Chatterjee, D.; Wei, J.; Kvit, A.; Bammes, B.; Levin, B.; Bilhorn, R.; Voyles, P. An Ultrafast Direct Electron Camera for 4D STEM. *Microsc. Microanal.* **2021**, *27*, 1004–1006. doi:10.1017/S1431927621003809.
237. Leapman, R. D.; Cosslett, V. E. Extended Fine Structure Above the X-Ray Edge in Electron Energy Loss Spectra. *J. Phys. D: Appl. Phys.* **1976**, *9*, L29–L32. doi:10.1088/0022-3727/9/2/003.
238. Sarikaya, M.; Qian, M.; Stern, E. A. EXELFS Revisited. *Micron* **1996**, *27*, 449–466. doi:10.1016/S0968-4328(96)00044-3.
239. Hart, J. L.; Lang, A. C.; Cummings, R. B.; MacLaren, I.; Taheri, M. L. Direct Detection EELS at High Energy: Elemental Mapping and EXELFS. *Microsc. Microanal.* **2019**, *25*, 584–585. doi:10.1017/S1431927619003659.
240. Ryu, C. W.; Egami, T. Origin of Liquid Fragility. *Phys. Rev. E* **2020**, *102*, 042615. doi:10.1103/PhysRevE.102.042615.
241. Egami, T.; Shinohara, Y. Correlated Atomic Dynamics in Liquid Seen in Real Space and Time. *J. Chem. Phys.* **2020**, *153*, 180902. doi:10.1063/5.0024013.
242. Egami, T.; Ryu, C. W. Medium-Range Atomic Correlation in Simple Liquids. II. Theory of Temperature Dependence. *Phys. Rev. E* **2021**, *104*, 064110. doi:10.1103/PhysRevE.104.064110.
243. Lieou, C. K.; Egami, T. Mean-Field Model for the Curie-Weiss Temperature Dependence of Coherence Length in Metallic Liquids. *Phys. Rev. E* **2022**, *105*, 044135. doi:10.1103/PhysRevE.105.044135.
244. Egami, T.; Ryu, C. W. World beyond the Nearest Neighbors. *J. Phys. Condens. Matter.* **2023**, *35*, doi:10.1088/1361-648X/acbe24.
245. Egami, T.; Ryu, C. W. Origin of Medium-Range Atomic Correlation in Simple Liquids: Density Wave Theory. *AIP Adv.* **2023**, *13*, doi:10.1063/5.0159044.
246. Paradis, P. F.; Ishikawa, T.; Yoda, S. Noncontact Density Measurements of Tantalum and Rhenium in the Liquid and Undercooled States. *Appl. Phys. Lett.* **2003**, *83*, 4047–4049. doi:10.1063/1.1624475.
247. Mukherjee, S.; Schroers, J.; Zhou, Z.; Johnson, W. L.; Rhim, W. K. Viscosity and Specific Volume of Bulk Metallic Glass-Forming Alloys and Their Correlation with Glass Forming Ability. *Acta Mater.* **2004**, *52*, 3689–3695. doi:10.1016/j.actamat.2004.04.023.
248. Poe, B. T.; McMillan, P. F.; Coté, B.; Massiot, D.; Coutures, J. Structure and Dynamics in Calcium Aluminate Liquids: High-Temperature ^{27}Al NMR and Raman Spectroscopy. *J. Am. Ceram. Soc.* **1994**, *77*, 1832–1838. doi:10.1111/j.1151-2916.1994.tb07058.x.
249. Massiot, D.; Trumeau, D.; Touzo, B.; Farnan, I.; Rifflet, J. C.; Douy, A.; Coutures, J. P. Structure and Dynamics of $CaAl_2O_4$ from Liquid to Glass: A High-Temperature ^{27}Al NMR Time-Resolved Study. *J. Phys. Chem.* **1995**, *99*, 16455–16459. doi:10.1021/j100044a038.
250. Sandor, M. T.; Kecskes, L. J.; He, Q.; Xu, J.; Wu, Y. Correlation of Mechanical Properties in Bulk Metallic Glasses with ^{27}Al NMR Characteristics. *Chin. Sci. Bull.* **2011**, *56*, 3937–3941. doi:10.1007/s11434-011-4834-z.
251. Xu, W.; Sandor, M. T.; Yu, Y.; Ke, H. B.; Zhang, H. P.; Li, M. Z.; Wang, W. H.; Liu, L.; Wu, Y. Evidence of Liquid-Liquid Transition in Glass-Forming $La_{50}Al_{35}Ni_{15}$ Melt above Liquidus Temperature. *Nat. Commun.* **2015**, *6*, 7696. doi:10.1038/ncomms8696.
252. Li, L.; Schroers, J.; Wu, Y. Crossover of Microscopic Dynamics in Metallic Supercooled Liquid Observed by NMR. *Phys. Rev. Lett.* **2003**, *91*, 265502. doi:10.1103/PhysRevLett.91.265502.
253. Russo, J.; Romano, F.; Tanaka, H. Glass Forming Ability in Systems with Competing Orderings. *Phys. Rev. X* **2018**, *8*, 21040. doi:10.1103/PhysRevX.8.021040.
254. Yu, Q.; Wang, X. D.; Su, Y.; Cao, Q. P.; Ren, Y.; Zhang, D. X.; Jiang, J. Z. Liquid-to-Liquid Crossover in the GaIn Eutectic Alloy. *Phys. Rev. B* **2017**, *95*, 1. doi:10.1103/PhysRevB.95.224203.
255. Su, Y.; Wang, X. D.; Yu, Q.; Cao, Q. P.; Ruett, U.; Zhang, D. X.; Jiang, J. Z. Temperature Dependent Structural Evolution in Liquid $Ag_{50}Ga_{50}$ Alloy. *J. Phys. Condens. Matter.* **2018**, *30*, 015402. doi:10.1088/1361-648X/aa996c.
256. Bian, X.; Wang, G.; Wang, Q.; Sun, B.; Hussain, I.; Zhai, Q.; Mattern, N.; Bednarčík, J.; Eckert, J. Cryogenic-Temperature-Induced Structural Transformation of a Metallic Glass. *Mater. Res. Lett.* **2017**, *5*, 284–291. doi:10.1080/21663831.2016.1263687.
257. Bian, X. L.; Wang, G.; Yi, J.; Jia, Y. D.; Bednarčík, J.; Zhai, Q. J.; Kaban, I.; Sarac, B.; Mühlbacher, M.; Spieckermann, F.; et al. Atomic Origin for Rejuvenation of a Zr-Based Metallic Glass at Cryogenic Temperature. *J. Alloy. Compd.* **2017**, *718*, 254–259. doi:10.1016/j.jallcom.2017.05.124.
258. Schawe, J. E. K.; Löffler, J. F. Existence of Multiple Critical Cooling Rates Which Generate Different Types of Monolithic Metallic Glass. *Nat. Commun.* **2019**, *10*, 1337. doi:10.1038/s41467-018-07930-3.
259. Römer, F.; Ramasamy, P.; Steffny, I.; Stoica, M.; Lienert, U.; Quick, C.; Hegedüs, Z.; Eckert, J.; Spieckermann, F. Crystallization of $Fe_{74}Mo_4P_{10}C_{7.5}B_{2.5}Si_2$ Metallic Glass: Insights from in-Situ Synchrotron Diffraction and Flash DSC. *Mater. Today Adv* **2025**, *25*, 100550. doi:10.1016/j.mtadv.2024.100550.



https://dspace.org/

From metallic liquids to metallic glasses: in-situ monitoring the atomic structure evolution by synchrotron X-ray diffraction

Stiehler, Martin E.; Georgarakis, Konstantinos

2025-12
Taylor & Francis
https://doi.org/10.1080/10408436.2025.2503148
Stiehler ME, Georgarakis K. (2025) From metallic liquids to metallic glasses: in-situ monitoring the atomic structure evolution by synchrotron X-ray diffraction. Critical Reviews in Solid State and Materials Sciences, Volume 50, Issue 6, December 2025, pp. 601-633

Downloaded from a DSpace repository. https://dspace.org/